

Transient stress evolution in repulsion and attraction dominated glasses

Christian P. Amann^{a)} and Matthias Fuchs^{b)}

Fachbereich Physik, Universität Konstanz, 78457 Konstanz, Germany

(Received 30 January 2014; final revision received 17 May 2014;
published 25 August 2014)

Synopsis

We present results from microscopic mode coupling theory generalized to colloidal dispersions under shear in an integration through transients formalism. Stress strain curves in start up shear, flow curves, and normal stresses are calculated with the equilibrium static structure factor as only input. Hard spheres close to their glass transition are considered, as are hard spheres with a short ranged square well attraction at their attraction dominated glass transition. The consequences of steric packing and physical bond formation on the linear elastic response, the stress release during yielding, and the steady plastic flow are discussed and compared to experimental data from concentrated model dispersions. © 2014 The Society of Rheology. [<http://dx.doi.org/10.1122/1.4881256>]

I. INTRODUCTION

Colloidal dispersions have been established as model systems in materials science. They behave like fluids at high dilution and form condensed phases if particle interactions dominate over entropic disorder. Equilibrium statistical mechanics explains equilibrium phases and their near-equilibrium properties based on direct particle interactions. While purely repulsive interactions lead to fluid and crystalline solids, attractions can also give rise to liquids. As colloidal dispersions offer the unique possibility to tailor the depth and range of the attractions, the conditions when liquid phases become stable could be established in studies, e.g., by [Lekkerkerker *et al.* \(1992\)](#). Yet colloidal dispersions also form various *metastable solid states* like fractal networks, particle gels, and glasses, which cannot be described with purely equilibrium statistical mechanics. They are important in industrial processes and products, and in biological systems, which generally are far from thermal equilibrium. The specific mechanical properties of the resulting soft solids are often tailored adjusting the competition between attractive and repulsive interactions. Various solid states, with very different elastic properties, have been prepared; recent studies include works by [Lu *et al.* \(2008\)](#), [Gibaud *et al.* \(2011\)](#), [Kim *et al.* \(2013\)](#), and others.

Mixtures of colloids with nonadsorbing polymers constitute one of the simplest systems, where effective interactions among the (larger) colloidal constituents can be adjusted in a controlled way. Two different glass states, viz., amorphous solids formed by

^{a)} Author to whom correspondence should be addressed; electronic mail: Christian.2.Amann@uni-konstanz.de

^{b)} Electronic mail: Matthias.Fuchs@uni-konstanz.de

the freezing-in of the cooperative structural dynamics, could be observed conclusively by [Pham *et al.* \(2002\)](#) and [Eckert and Bartsch \(2002\)](#), as had been predicted by [Fabbian *et al.* \(1999\)](#) and [Bergenholtz and Fuchs \(1999\)](#) using mode coupling theory (MCT). Controlling the range of the attraction proved crucial for the formation of “attraction driven glasses,” where particles form physical bonds to their neighbors. Attraction driven glasses require short-ranged attractions so that particles become tightly localized, as can be clearly seen in computer simulations [[Puertas *et al.* \(2002\)](#)]. In “repulsion driven glasses,” the cooperative behavior of the neighbors forming the cage localizes particles less tightly. The localization length there corresponds to Lindemann’s length [[Lindemann \(1910\)](#)] which is roughly a tenth of the average particle separation [[Hansen and McDonald \(2009\)](#)]. Lindemann had found that atomic displacements increase up to this value when (crystalline) solids are heated to their melting temperature. Mode coupling theory as developed by [Götze \(2009\)](#) and others established that Lindemann’s length also characterizes the frozen-in structure of repulsion driven glasses, as was verified experimentally by [Pusey and van Meegen \(1987\)](#) and [van Meegen and Underwood \(1993\)](#) in colloidal hard sphere (HS) dispersions. As attractions change the structure of these glasses only if they are of short range MCT predicts that qualitative changes require attraction ranges (somewhat) shorter than Lindemann’s length and as attractions in molecular systems act across longer ranges, molecular glass transitions fall into the class of repulsion driven transitions. This has made HS colloids a model system for studying the glass transition in molecular, metallic, and simple supercooled liquids, which was recently reviewed by [Hunter and Weeks \(2012\)](#). Attraction driven glasses require attraction strengths of the order of only a few k_{BT} (thermal energies) and can form at particle concentrations lower than repulsive ones [[Dawson *et al.* \(2000\)](#)]. The aspect that increasing the strength of attraction at first destabilizes and melts the (repulsion driven) glass provides insight into the mechanism of vitrification and its theoretical description. For any strength, short-ranged attractions increase the equilibrium probability of close-particle contacts, viz., the contact value of the pair correlation function. Yet, this increased stickiness reduces the medium-ranged order in the disordered fluid as measured in the principal peak of the equilibrium structure factor. Mode coupling theory predicts that this decrease destabilizes the repulsion driven cages so that a HS glass melts upon turning on a narrow attraction. This causes an appreciable shift of the glass transition to higher concentrations. In a recent investigation, [Willenbacher *et al.* \(2011\)](#) achieved a shift of the transition packing fraction by more than 10%. For fixed concentration, short-ranged attractions then cause a glass transition when at increasing attraction strength large wavevector contributions in the equilibrium structure factor contribute strongly. Inbetween, a re-entrant fluid region lies where equilibrium is approached at long times. The continuation of this states diagram to lower concentrations, where colloidal gels are observed [[Lu *et al.* \(2008\)](#)], remains an active area of research. For example, computer simulations investigate it by following the temporal evolution of the average localization length of individual particles as function of concentration [[Zaccarelli and Poon \(2009\)](#)].

Metastable glassy systems exhibit a complex interplay between their structural relaxation and flow causing a strongly nonNewtonian response. Moreover, the structural and mechanical changes during or after processing using flow or other external fields also are crucial for achieving desired material properties. Thixotropy and ageing are important and are moving into the reach of first principles theories only recently [[Ballauff *et al.* \(2013\)](#)]. While a number of studies exist of the mechanical response of dispersions approaching the repulsion driven glass transition a recent one [[Siebenbürger *et al.* \(2009\)](#)] where the transition density could be approached very closely is reviewed by [Siebenbürger *et al.* \(2012\)](#) there are far fewer studies of the nonlinear rheology in the

complete region covering repulsion and attraction driven glass transitions. Besides the already mentioned work by Willenbacher *et al.* (2011) combining rheology and dynamic light scattering, especially the seminal investigations by Pham *et al.* (2006) and Pham *et al.* (2008) provided insights into the nonlinear mechanical behavior under different rheological protocols and varying repulsive and attractive effects by varying concentration and attraction strength. As also seen in computer simulations by Puertas *et al.* (2007), the linear shear moduli are far larger at the attraction driven glass transition than at the repulsion driven one. In MCT, this arises from the dominance of large wavevectors in the approximated Green-Kubo relation for the linear moduli, which predicts an increase with the square of the inverse of the relative attraction range in the sticky limit [Bergenholtz *et al.* (2000)]. Another intriguing observation by Pham and coworkers concerns the yielding of glasses under applied strain. A typical strain of around 10%–20% characterizes the shear-induced yielding of repulsion driven glasses when experiencing step strain and start-up flow, while attraction driven glasses yield in a two-step process. The former observation, in agreement with light scattering studies under large amplitude oscillatory shearing by Petekidis *et al.* (2002), nicely ties to the picture of the cage effect and its characteristic length following Lindemann's criterion; yet this connection has not been established theoretically up to now. The second observation, already visible in oscillatory shear experiments by Gadala-Maria and Acrivos (1980) and supported by a detailed investigation under start-up shear flow by Koumakis and Petekidis (2011), cannot be interpreted so easily by the cage picture because the two characteristic strain values are around 10% and 100%. The second value is far larger than the local cage picture would imply, and the attraction range, which was around 5% in the experimental system, appears not to characterize the stress-strain relations.

Aim of the present contribution is to determine the stress-strain relations close to repulsion and attraction driven glass transitions from MCT as generalized to sheared colloidal dispersions in the integration-through-transients (ITT) framework. We will consider the quintessential repulsive glass transition, viz., the one in a HS fluid, and a typical attraction driven one for a narrow square-well pair potential. Specifically, we will consider start-up shear flow with fixed shear rate and determine the transient shear stress as function of accumulated strain. In the generalization of the microscopic MCT developed by Brader *et al.* (2012) based on the work by Fuchs and Cates (2002), the structural relaxation under arbitrary, homogeneous, and incompressible flows is deduced from the equilibrium structure factor so that caging and bond formation, as in the quiescent situation, can be discussed.

Our work bears similarity to the study by Henrich *et al.* (2009) where hard disks were considered in two dimensions. Here, we present the first calculations within microscopic MCT-ITT for HSs in three dimensions and additionally consider attractive glasses in the second part. Our work also bears some similarity to the one by Miyazaki *et al.* (2004), who, however, concentrated on fluid states under shear and on time-dependent fluctuations around the steady state. We focus here on the transient dynamics of yielding glass states and their stationary, time-independent properties which are not accessible to the theory by Miyazaki *et al.* (2004). Our work also bears similarity to the study by Priya and Voigtman (2014), who also consider the nonlinear rheology of repulsion and attraction dominated glass (ADG) transitions. They use a simplified MCT-ITT, where shear deformations are isotropically averaged, which enables them to study wider variations in the attraction ranges and strengths than possible in our solution of MCT-ITT without additional approximations.

In Sec. II, the pertinent equations of MCT are summarized. Section III gives an overview of the studied systems and the glass states diagram, while Secs. IV and V describe the results for HSs without and with square-well attraction, respectively. Section VI concludes with a comparison of the findings with experimental data.

II. NONLINEAR RHEOLOGY WITH MODE COUPLING THEORY

The ITT formalism which generalizes MCT to driven systems provides a method to calculate the complete time evolution of a concentrated dispersion under homogeneous strain deformation. This yields more information than, e.g., just obtaining the steady state properties as the evolution from elastic to plastic response can be observed. The MCT-ITT approach by [Brader *et al.* \(2012\)](#) is presently restricted to incompressible flows and neglects hydrodynamic interactions. We will consider start-up shear flows, which is a simple time-dependent deformation protocol where the former condition is obeyed, and high particle concentrations, where the dominance of structural correlations motivates our neglect of hydrodynamics. Solvent effects are presumed to renormalize the hydrodynamic radii and short time diffusion coefficients.

Microscopic starting point is the Smoluchowski equation for interacting Brownian particles in a given shear flow. The particles' time evolution follows from affine motion with the flow and random motion causing nonaffine displacements, both combined in the Smoluchowski operator

$$\Omega = \sum_{i=1}^N \frac{\partial}{\partial \mathbf{r}_i} \cdot \left[\frac{\partial}{\partial \mathbf{r}_i} - \mathbf{F}_i - \dot{\gamma} y_i \hat{\mathbf{x}} \right]. \quad (1)$$

The force on particle i derives from a potential, where the chosen pair interaction will enter in Secs. III V. Dimensionless units are used, where length, energy, and time are measured in units of particle diameter d , thermal energy k_{BT} , and d^2/D_0 , respectively. The effect of shear relative to Brownian motion is measured by the bare Péclet number $Pe_0 = \dot{\gamma} d^2/D_0$, which in these units agrees with the shear rate. Note that the Weissenberg number $Wi = \dot{\gamma} \tau$, with τ an intrinsic α -relaxation time scale of a fluid, is also called (dressed) Péclet number Pe . Viscoelastic response can be observed at $Pe_0 \ll 1$ and $Wi \gtrsim 1$, while the response for $Wi \ll 1$ is the one of a Newtonian fluid.

An equation of motion for a *transient* density correlator $\Phi_{\mathbf{q}}(t)$ encodes rapid local motion without structural decay, and elasticity and plasticity owing to structural rearrangements. The transient density correlator $\Phi_{\mathbf{q}}(t) = \langle \rho_{\mathbf{q}}^* \rho_{\mathbf{q}}(t) \rangle / NS_q$, is the correlation function built with density fluctuation, $\rho_{\mathbf{q}} = \sum_{j=1}^N \exp\{i\mathbf{q} \cdot \mathbf{r}_j\}$. Their time evolution is given by the adjoint of the Smoluchowski operator from Eq. (1), $\rho_{\mathbf{q}}(t) = e^{\Omega^\dagger t} \rho_{\mathbf{q}}$. In ITT, the average can be performed over the equilibrium Gibbs-Boltzmann ensemble, because the system is assumed to be in equilibrium initially. Thus the normalization, giving $\Phi_{\mathbf{q}}(0) = 1$, is done with the equilibrium structure factor S_q . The *shear-advected* wavevector $\mathbf{q}(t) = (q_x, q_y - \dot{\gamma} t q_x, q_z)^T$ appearing in the definition accounts for the affine particle motion with the flow and gives $\Phi_{\mathbf{q}}(t) \equiv 1$ in the absence of nonaffine motion. Random motion, affected by the shear flow, causes $\Phi_{\mathbf{q}}(t)$ to decay. In MCT-ITT, this is given by an equation of motion containing a retarded friction kernel which arises from the competition of particle caging and shear advection of fluctuations

$$\dot{\Phi}_{\mathbf{q}}(t) + \Gamma_{\mathbf{q}}(t) \left\{ \Phi_{\mathbf{q}}(t) + \int_0^t dt' m_{\mathbf{q}}(t, t') \dot{\Phi}_{\mathbf{q}}(t') \right\} = 0. \quad (2)$$

The initial decay rate contains Taylor dispersion as $\Gamma_{\mathbf{q}}(t) = q^2(t)/S_{q(t)}$. The generalized friction kernel $m_{\mathbf{q}}(t, t')$ is an autocorrelation function of fluctuating stresses. Based on the insights of quiescent MCT as described by [Götze \(2009\)](#), it is approximated by a quadratic polynomial in the density correlators

$$m_{\mathbf{q}}(t, t') = \int \frac{d^3 k}{(2\pi)^3} \frac{n S_{q(t)} S_{k(t')} S_{p(t')}}{2q^2(t) q^2(t')} V_{\mathbf{qk}}(t) V_{\mathbf{kp}}(t') \Phi_{\mathbf{k}}(t) \Phi_{\mathbf{p}}(t'), \quad (3)$$

with abbreviation $\mathbf{p} = \mathbf{q} - \mathbf{k}$, and n the particle density. The vertex function is given by

$$V_{\mathbf{q}\mathbf{k}\mathbf{p}}(t) = \mathbf{q}(t) \cdot (\mathbf{k}(t) c_{k(t)} + \mathbf{p}(t) c_{p(t)}), \quad (4)$$

where c_k is the Ornstein-Zernicke direct correlation function, $c_k = (1 - 1/S_k)/n$. These equations of motion were derived in detail by Fuchs and Cates (2009) using a Zwanzig-Mori projection-operator formalism together with mode coupling approximations. The iterative solving algorithm for Eqs. (2) (4) is discussed in the Appendix. The equilibrium structure factor, S_k , encodes the particle interactions and introduces the experimental control parameters like density and temperature. Again generalizing quiescent MCT to flow, the potential part of the stress $\sigma_{\alpha\beta}(\dot{\gamma}) = \langle \sigma_{\alpha\beta} \rangle^{(\dot{\gamma})}/V$ is approximated assuming that stress relaxations can be computed from integrating the transient density correlations

$$\sigma_{xy}(t) = \dot{\gamma} \int_0^t dt' \int \frac{d^3k}{(2\pi)^3} \left[\frac{k_x^2 k_y(-t') k_y S'_k S'_{k(-t')}}{k k(-t') S_k^2} \right] \Phi_{\mathbf{k}(-t')}^2(t'). \quad (5)$$

Equation (5) is the central equation which we will evaluate for different systems. It can also be used to derive a constitutive equation for the shear stress of the form $\sigma_{xy}(t) = \dot{\gamma} \int_0^t dt' g_{xy}(t', \dot{\gamma})$ with a *generalized shear modulus*

$$g_{xy}(t, \dot{\gamma}) = \frac{1}{2} \int \frac{d^3k}{(2\pi)^3} \left[\frac{k_x^2 k_y k_y(t) S'_{k(t)} S'_k}{k(t) k S_{k(t)}^2} \right] \Phi_{\mathbf{k}}^2(t). \quad (6)$$

Here, a shift of the integration variable was performed collecting the wavevector advection in a time-dependent vertex (the term in the square bracket) which is weighted with the square of the density correlator at wavevector \mathbf{k} . Without wavevector advection, $g_{xy}(t, \dot{\gamma} = 0)$ recovers the quiescent MCT expression for the stress autocorrelation function [Götze (2009)]; see a review by Fuchs (2010) for more discussions. For an ideal elastic solid, the modulus g_{xy} would be constant and stress and accumulated strain $\dot{\gamma}t$ would be proportional. If $g_{xy}(t)$ does not depend on $\dot{\gamma}$ and decays on an intrinsic time scale τ , the finite time integral over $g_{xy}(t)$ is the long time viscosity η_{xy}^0 of a Newtonian fluid, stress, and shear rate are then proportional. This recovers Maxwell's model of linear response. Viscoelastic media exhibit a nonlinear behavior in $\dot{\gamma}$, because of a $\dot{\gamma}$ functionality of $g_{xy}(t, [\dot{\gamma}])$. MCT can obviously provide a microscopic description of such viscoelasticity. Equation (6) will be studied in Secs. IV V specifying different systems by implementing different equilibrium structure factors.

III. OVERVIEW OF CONSIDERED REPULSIVE AND ATTRACTIVE SYSTEMS AND THEIR QUIESCENT GLASS STATES

In MCT-ITT, the structural relaxation is determined by the direct correlation function c_q (equivalently the equilibrium structure factor S_q) which describes the effective interaction between density fluctuations. In density functional theory, it gives the quadratic term in the interaction part of the free energy functional; in MCT it enters the interaction vertices when fluctuating stresses are connected to density fluctuations. As discussed in detail by Dawson *et al.* (2000), there are two major mechanisms for vitrification in the self-consistency equations of MCT for pair potentials consisting of an excluded volume core and a short-ranged attraction. They can be discerned from the wavevector range where the major contributions arise in the memory kernel of Eq. (3).

The normal situation is that the principal peak in S_q dominates, and that the glass transition is crossed when it becomes high. This glass transition originates in the local ordering caused by the excluded volume constraints in dense fluids, the transition leads to a “repulsion dominated glass” (RDG), and the width of the glass form factor f_q in reciprocal spaces is set by the localization length following Lindemann’s criterion. The inset of Fig. 1 shows the glass form factor f_q^c at the transition of a fluid of monodisperse HSs, which is the most simple example for this transition [Götze (2009)]. Solving Eqs. (2)–(4) numerically at vanishing shear rate and using the Percus-Yevick (PY) approximation for the structure factor, the transition lies at packing fraction $\phi_c = 0.515712(1)$, which is somewhat below the value $\phi_c = 0.58$ established in experiment for slightly polydisperse HS colloids [Pusey and van Meegen (1987); Hunter and Weeks (2012)]. The present numerical result for ϕ_c and especially f_q^c (e.g., the small wiggles close to the second and third peaks) differ from more precise calculations reviewed by Götze (2009), because the chosen discretization of the wavevector integrals in Eq. (3) is optimized to handle the anisotropic distortions under shear, including with attractions. Presently, we cannot choose a finer discretization, because a single stress vs strain curve (from Fig. 4) takes 90 h running time on a modern CPU.

A second mechanism causes arrest of the structural relaxation when a short-ranged attraction is strong enough in a colloidal dispersion. A square-well potential (SWP) of width Δ and attractive depth u_0 is chosen here to exemplify this. It acts outside the excluded volume core. This study extends the one by Dawson *et al.* (2000) by including shear flow. The potential depth will be made dimensionless using thermal energy k_{BT} , i.e., $U = u_0/k_{BT}$. Relative attraction ranges $\delta = \Delta/d$ smaller than Lindemann’s ratio $\delta < 0.1$ are required which cause strong contributions in the memory kernel of Eq. (3) at large wavevectors. The “ADG” transition takes place when wavevectors of the order $k \sim 1/\Delta$ dominate. The resulting glass form factors f_q extend to large wavevectors and their

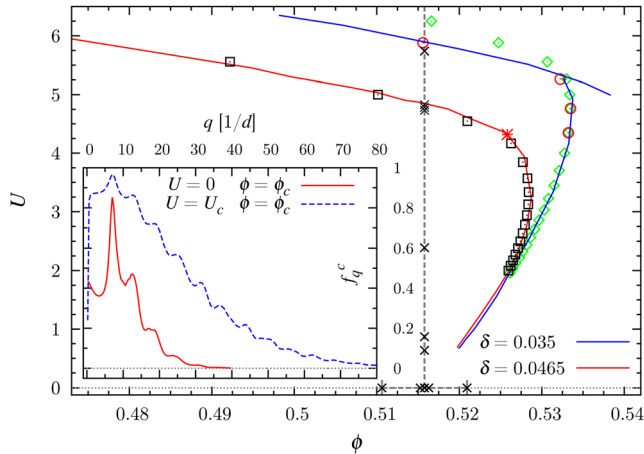


FIG. 1. Main panel: States diagram showing the critical glass transition interaction strength $U_c = u_0/k_{BT}$ and packing fraction ϕ_c for HSs with square well attraction. The lines are taken from Dawson *et al.* (2000); see the legend for the relative attraction range of the SWP $\delta = \Delta/d$, with Δ attraction range and d particle diameter. A star marks the higher order glass transition point A_4 at $U = U_{A_4}$. The symbols mark ADG calculations, with $q_{\max} = 79.8$ (black squares and green diamonds) or $q_{\max} = 119.8$ (red circles). Calculations (marked by symbols \times) along two paths crossing a glass transition will be discussed later: Crossing the HS transition increasing ϕ for $U = 0$, and crossing the ADG increasing U at ϕ_c . The inset shows (isotropic) nonergodicity parameters f_q^c at the two transitions, viz., at the critical packing fraction ϕ_c for $U = 0$ (HS case) and $U = U_c$ (attraction driven transition).

q -dependent width corresponds to a localization length of the order of the attraction range Δ . This is shown in the inset of Fig. 1, where the form factors f_q^c are shown at the attraction driven glass transition at $U_c = 4.7811(8)$ and $\delta = 0.0465$ at the same packing fraction ϕ_c as the HS transition; the different widths at the HS and ADG transitions are apparent.

The complete glass transition lines (states diagram) in Fig. 1 for two attraction ranges verify that the first effect when turning on a short-ranged attraction is a destabilization of the RDG. The glass transition line moves to higher packing fractions initially with increasing attraction strength U . The effect is stronger for smaller relative attraction range δ . A reentrant fluid region emerges which extends up to a maximal packing fraction, around where the two glass transition lines merge or intersect. The scenario depends on the precise attraction range. For $\delta = 0.0465$ both transition lines merge in an A_4 singularity, while for shorter ranges both glass transition lines intersect at a crossing point, and the ADG ends at an A_3 singularity [Dawson *et al.* (2000)].

In the present study, the transient stress evolution close to two typical transitions of both kinds shall be explored. Numerical calculations will be performed for two paths, one varying the concentration at fixed (vanishing) attraction strength, and the other one at fixed packing fraction for increasing well depth. Equilibrium structure factors, which are the only input to the theory, will be taken from the work by Dawson *et al.* (2000). While the choice of $U = 0$ is quite natural and leads to the pure HS system, qualitatively similar results would hold for all RDG transitions at fixed U (much) smaller than the attraction strength of the A_4 singularity. The second transition to the ADG is chosen for the same packing fraction as the HS transition in order to eliminate density dependent differences. According to MCT qualitatively similar results would hold for all ϕ below the density of the A_4 singularity. In order to achieve a clear time scale separation between the slow structural relaxation of interest and the fast local dynamics, small relative separations from the glass transitions shall be considered. They will be expressed using the relative separations $\varepsilon = (\phi - \phi_c)/\phi_c$ and $\varepsilon_U = (U - U_c)/U_c$, respectively.

IV. HS TRANSITION

After the presentation of the MCT equations and a short overview of the quiescent glass states diagram, the yielding of HS glasses under applied shear strain shall be discussed first. It gives the example relevant to concentrated dispersions without especially short-ranged attractions, and to molecular and metallic glass-forming liquids.

Equation (5) is a constitutive equation for the shear stress undergoing simple shear after start-up at $t = 0$. The vertex (the term in the square bracket) depends on time only via the accumulated strain, $\gamma = \dot{\gamma}t$. The squared correlators depend on time and accumulated strain independently in general and thus the stress-strain relations obtain different forms depending on the bare Péclet number Pe_0 and the distance to the glass transition ε . The numerical calculation proceeds by first solving the self-consistency equations (2) (4) for the density correlators $\Phi_q(t)$ at given shear rate $\dot{\gamma}$, and second by integrating Eq. (6) to obtain the generalized shear modulus. If desired, flow-curves and stress-strain relations can then be obtained.

Figures 2 and 3 provide a good qualitative illustration of the transient stress regime, as well as already the quantitative data. Figure 2 shows the shear stress vs strain. Figure 3 shows the generalized shear modulus. Three regimes of viscoelasticity can be identified from the curves:

(i) First, the stress grows linearly with strain proportional to an elastic shear modulus G_∞ . This expresses Hooke's law, $\sigma_{xy} = G_\infty \gamma$. Figure 3 shows that this corresponds to a plateau in $g_{xy}(t, \dot{\gamma})$ for intermediate times. It is reached after some shear-rate independent

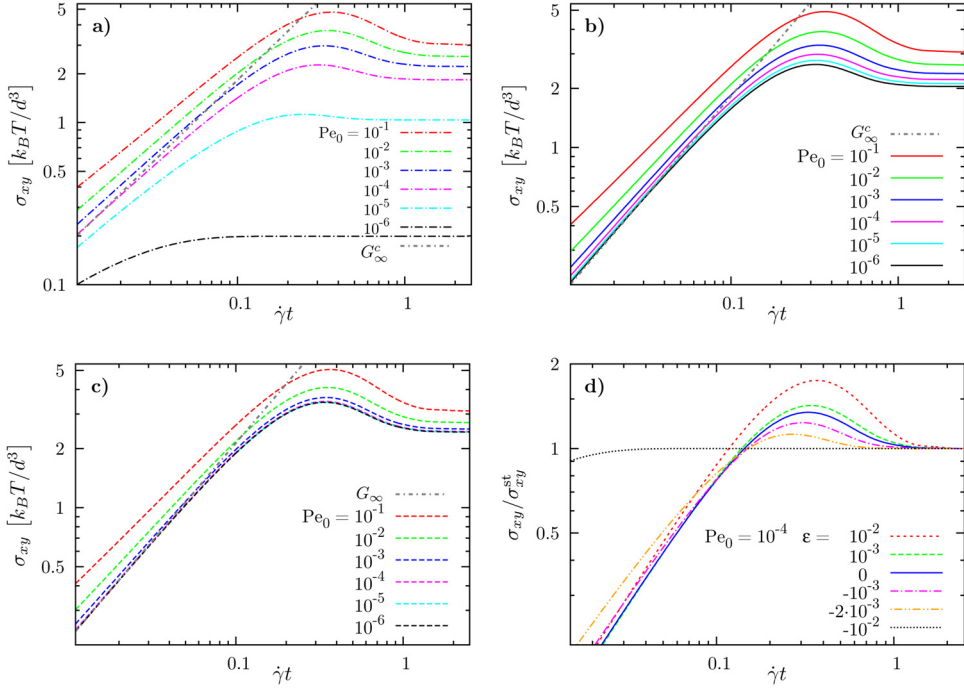


FIG. 2. Transient shear stress σ_{xy} as a function of accumulated strain γt for several separation parameters ε ($\phi - \phi_c$)/ ϕ_c and bare Péclet numbers Pe_0 calculated for a HS system (see legends for Pe_0). Panel (a) is in the fluid, $\varepsilon = 10^{-3}$, (b) at the transition, $\varepsilon = 0^+$, and (c) in the glass, $\varepsilon = 10^{-3}$. The elastic moduli G_∞ and G_∞^c , calculated from the plateaus of Fig. 3, are shown as gray, dashed dotted lines. Panel (d) shows stress curves rescaled by the steady state value varying ε at constant $Pe_0 = 10^{-4}$.

short-time relaxation and holds up to the final decay time. This plateau has the value G_∞ . The index ∞ can be understood to refer to an infinite intrinsic relaxation time, which characterizes an elastic solid. In fluid states, the intrinsic final structural or α -relaxation causes a decay of $g_{xy}(t, \dot{\gamma} = 0)$, which softens the stress-strain relations. See Fig. 2(a), where $\sigma_{xy}(t)$ becomes smaller at low shear rates, i.e., it becomes plastic because $\dot{\gamma} \tau < 1$. There is a loss of memory in the system, causing deviations from the linear elastic and leading to a viscous response. At times long compared to the intrinsic α -relaxation time τ , a Newtonian viscosity is observed, $\sigma_{xy}(t \gg \tau) \rightarrow \eta_{xy}^0 \dot{\gamma}$. Above the glass transition, MCT predicts that the glass structure is persistent and that the plateau does not decay (ideal glass), which is an idealization which is not observed experimentally. Nevertheless, the time-window where the shear modulus is nearly time-independent can be made arbitrarily large by supercooling further. In MCT, the frozen-in glass structure is the reason for solid elasticity. Increasing the shear rate, the shear-distorted structure of the HSs inside their yielding structural cages stores additional stress. This increase of $\sigma_{xy}(\gamma)$ at small strains is an “anelastic” effect in the β -process of MCT, which describes the instability of the cages trapping the particles [Voigtmann *et al.* (2012)]; this can be seen best in panels (b) and (c) of Fig. 2.

(ii) Shear-induced decay melts the glass, viz., the G_∞ -plateau decays after a decay time proportional to the inverse of the shear rate; see Fig. 3. Consequently the time integral in Eq. (5), viz., the area under $g_{xy}(t)$ vs time, does not increase anymore. A steady state value of $\sigma_{xy}(t)$ is reached in Fig. 2 at strains of order one, denoted as flow curve value $\sigma_{xy}^{st}(\dot{\gamma})$; see Fig. 4 for the flow curve. The approach to a steady flow curve requires plastic

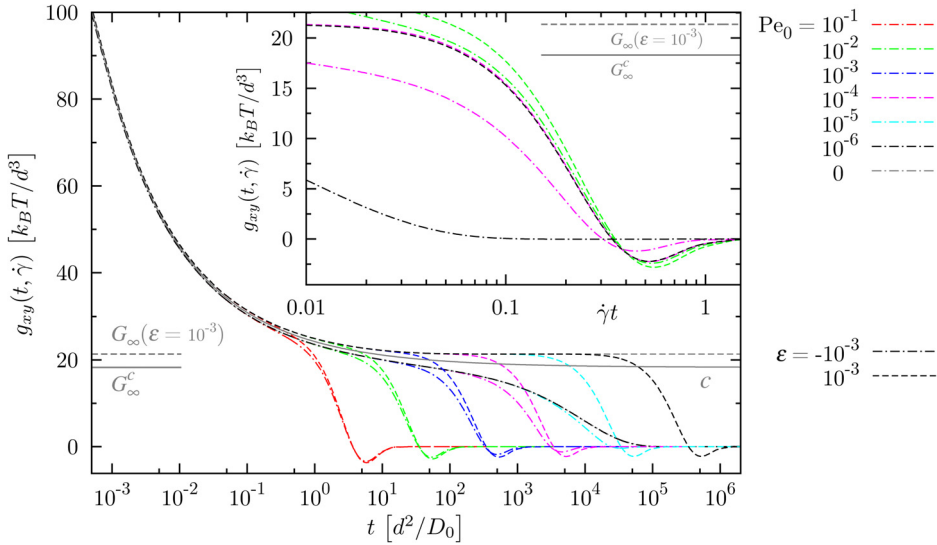


FIG. 3. Generalized shear modulus $g_{xy}(t, \dot{\gamma})$, Eq. (6), as function of time (*main panel*) and accumulated strain (*inset*; sets for every second Pe_0 left out for clarity). The legend provides *color coded* the strain rates and *line style coded* the separation parameters ε ; a letter *c* labels the critical $g_{xy}(t, 0)$ for $\varepsilon = 0^+$. In the main panel, fluid curves at $Pe_0 = 0$ and 10^{-6} overlap, in the inset glass curves at $Pe_0 = 10^{-6}$ and 10^{-4} overlap. Elastic shear moduli $G_\infty(\varepsilon)$ can be read off from quiescent curves ($Pe_0 = 0$), with $G_\infty(0^+) = G_\infty^c = 18.3 k_B T / d^3$ and $G_\infty(10^{-3}) = 21.4 k_B T / d^3$. The *inset* shows subtle differences in the typical strain γ_* , where $g_{xy} = 0$, when shear driven and internal relaxation in $\Phi_q(t, \gamma)$ interfere. This becomes most clear for $Pe_0 = 10^{-6}$ in the fluid phase, where the internal relaxation dominates and the undershoot disappears.

effects, which cause the final decay of $g_{xy}(t)$. For increasing Pe_0 , the plateau decay starts earlier and the short-time relaxation becomes more important.

(iii) Between the steady-state regime of the flow curve and the elastic regime occurs a transient plastic regime. From Fig. 3 can be verified that $g_{xy}(t)$ takes negative values prior to its final decay to zero. This negative area under the $g_{xy}(t)$ curve adds a negative portion to $\sigma_{xy}(t)$ so that the stress decreases onto the steady-state plateau. The emerging bump in Fig. 2 is called stress overshoot. The stress is maximal for the peak strain value γ_* , i.e., Eq. (5) identifies γ_* as the zero of $g_{xy}(\gamma = \dot{\gamma}t)$. If, in the fluid phase, the structural relaxation time τ is smaller than the shear-induced one, the stress overshoot vanishes; Fig. 2(a) illustrates this. This agrees with a result from linear response theory, viz., that the equilibrium shear modulus $g_{xy}(t, \varepsilon < 0)$ is completely monotone [Götze (2009)] and is observed in experiments on colloidal dispersions by Koumakis *et al.* (2012b), Koumakis *et al.* (2012a), and Amann *et al.* (2013).

Figure 4 shows the flow curve values $\sigma_{xy}^{st}(\dot{\gamma}) = \sigma_{xy}(t \rightarrow \infty, \dot{\gamma})$ of the steady-state regime of the stress-strain curves from Fig. 2 and also the long-time shear viscosity $\eta_{xy} = \sigma_{xy}^{st} / \dot{\gamma}$. The difference between fluid phase and glass phase in the context of MCT can be seen. In the glass phase and for $Pe_0 \rightarrow 0$, the area under $g_{xy}(t)$ becomes proportional to $1/\dot{\gamma}$. In consequence, a constant dynamic yield stress σ_{xy}^+ can be read off directly from the flow curve for vanishing shear rate, $\sigma_{xy}^+ = \sigma_{xy}^{st}(\dot{\gamma} \rightarrow 0, \varepsilon \geq 0)$. This stress is necessary to keep the glass yielding and flowing at infinitesimally small shear rates. Because this yield stress is nonzero, the Newtonian viscosity diverges in the glass. Increasing the shear rate, processes on intermediate time scales [including the β -process in MCT studied by Götze (2009)] cause the stress to become larger. The β -process is slowest close to the glass transition, and therefore the flow curve at $\varepsilon = 0$ varies sensitively with shear rate

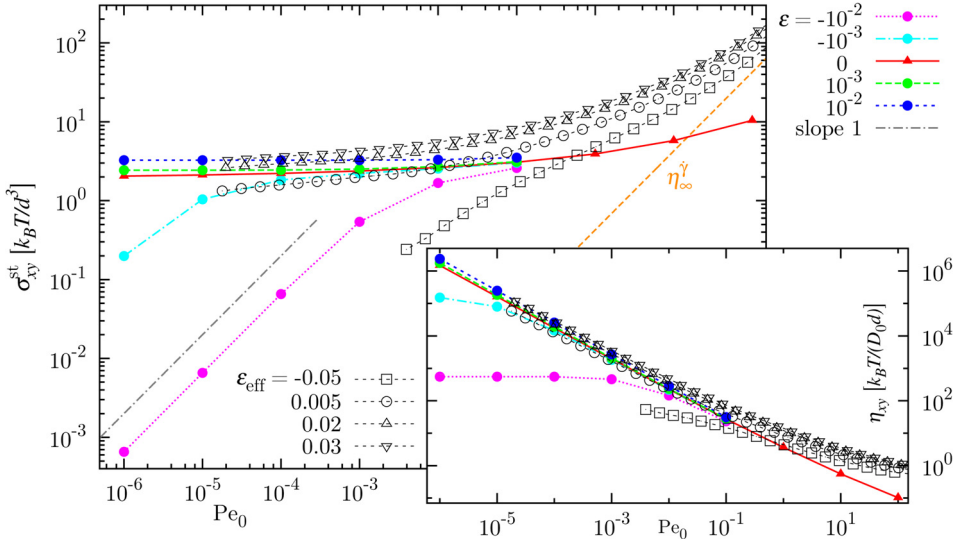


FIG. 4. The *main panel* shows flow curves $\sigma_{xy}(t \rightarrow \infty) = \sigma_{xy}^{\text{st}}$ vs bare Péclet number Pe_0 for separation parameters $\varepsilon = (\phi - \phi_c)/\phi_c$ as given in the legend. The *colored, full symbols* denote numerically obtained values for six shear rates $Pe_0 = 10^{\{-6, \dots, -1\}}$ which are connected with straight lines as guides to the eye. For $\varepsilon = 0^+$, higher Pe_0 were calculated up to the failure of the numerics at $Pe_0 \geq 10^1$; the $Pe_0 = 10^2$ point was computed without friction kernel in Eq. (2) (i.e., just Taylor dispersion). The *black, hollow symbols* with effective separation parameters ε_{eff} given in the legend are experimental data obtained by [Crassous et al. \(2008\)](#); the separation parameters ε_{eff} were deduced from loss $G''(\omega)$ and elastic $G'(\omega)$ spectra. The measured effective packing fractions were $\phi_{\text{eff}} = 0.540, 0.580, 0.608, \text{ and } 0.622$. A *gray, dashed dotted line* illustrates a slope of 1 and thus the Newtonian regime. The high shear viscosity $\eta_{\infty}^{\dot{\gamma}}$ indicates the hydrodynamic contribution [$\eta_{\infty}^{\dot{\gamma}} = 1.56k_B T / (D_0 d)$] as measured by [Crassous et al. \(2008\)](#) neglected in the MCT ITT calculations. The comparison is discussed in Sec. VI. The *inset* shows the stationary viscosity $\eta_{xy} = \sigma_{xy}^{\text{st}} / \dot{\gamma}$.

already at very small Pe_0 . For a schematic model of MCT-ITT, [Hajnal and Fuchs \(2009\)](#) deduced a Herschel-Bulkley law at the transition, which unfortunately cannot be tested in our calculations because of the coarse discretization. Deeper in the glass, the flow curve stays rather constant, because the β -process has become faster, and σ_{xy}^+ can be observed for a wider window in Pe_0 . It must be distinguished from a static yield stress, which a static load would have to overcome to fluidize a glass. One could within this context try to identify the peak-stress observed during the overshoot as static yield stress, but the corresponding shear-protocol is shear-rate and not stress controlled. The static yield stress could be (and is) different if one increases the stress in a controlled manner until the glass starts to flow. The issue of creep does then arise, which can be modeled with a stress controlled MCT as shown by [Siebenbürger et al. \(2012\)](#).

If in the fluid phase ($\varepsilon < 0$), the shear-rate independent structural decay characterized by the quiescent α -time τ takes place much earlier than the shear-induced one at time $1/\dot{\gamma}$, the integral in Eq. (5) becomes shear-rate independent and leads to the Newtonian viscosity η_{xy}^0 . The linear relation between stress and shear rate defines a Newtonian fluid, and more generally, the Newtonian viscosity is defined in the limit $Wi = \dot{\gamma}\tau \rightarrow 0$. A first Newtonian plateau can be identified for fluid states in Fig. 4 inset. A second Newtonian plateau would arise if the initial decay $\Gamma_q(t)$ in Eq. (2) gave a rapid shear-rate independent decay of the transient correlators at high shearing. This would also make $g_{xy}(t)$ independent from $\dot{\gamma}$ for high shear rates, viz., $Pe_0 \ll 1$. The present MCT-ITT cannot address this, as it describes the physics of structural arrest at long times and uses for short-times the quiescent S_q and Brownian motion with D_0 as input without further considering how

shear might affect them prior to structural arrest. Another problem arises, because the actual numerical iteration algorithm becomes unreliable for $Pe_0 > 10$. The flow curve becomes nonmonotonic for stronger shear rates and can even turn negative for some parameter values.

How a stress overshoot emerges in microscopic MCT has been discussed already for a simplified model with isotropic shear-distortions by Zausch *et al.* (2008) and for schematic MCT by Amann *et al.* (2013). It provides insights into the physical mechanisms involved in the yielding of glass. These will be discussed in more detail in context with Fig. 12 comparing effects from repulsion and attraction. Here, the pertinent results for HSs shall be summarized. The peak in the transient stress indicates a characteristic strain value γ_* for the yielding process of a glass because it only arises for $Wi \gg 1$. Another quantity, the relative peak amplitude, $\sigma_{xy}^{pk}/\sigma_{xy}^{st} - 1$, characterizes the stress built-up during the linear response of the glass, which is released during the later stage of the yielding process.

Numeric evaluations for the present HS system lead to the dependence of the peak strain γ_* , viz., the zero of $g_{xy}(t, \dot{\gamma})$, on shear rate and packing fraction, which is shown in Fig. 5. One verifies that in the glass ($\varepsilon > 0$) and for small Pe_0 , the critical yield strain γ_* is independent of shear rate. The reason is that intrinsic time scales then play no role in Eq. (5), because the transient density correlators decay with accumulated strain, as does the vertex in any case. If the transient density correlators, which encode the structural relaxation, vary with time (and wavevector) even for negligible accumulated strain, then the value of γ_* changes due to the dependence of the integral on the whole \mathbf{k} -range. When the linear response regime of the fluid dispersion is approached, the stress overshoot vanishes, so that the zero of $g_{xy}(t)$ still can be used to define γ_* , but it loses its role as position of a noticeable overshoot in the stress-strain curve. The inset in Fig. 5 shows the vanishing of the relative overshoot height for negative separation parameters, $\varepsilon < 0$. Only if the Weissenberg number $Wi = \dot{\gamma}\tau$ exceeds unity, a well developed stress

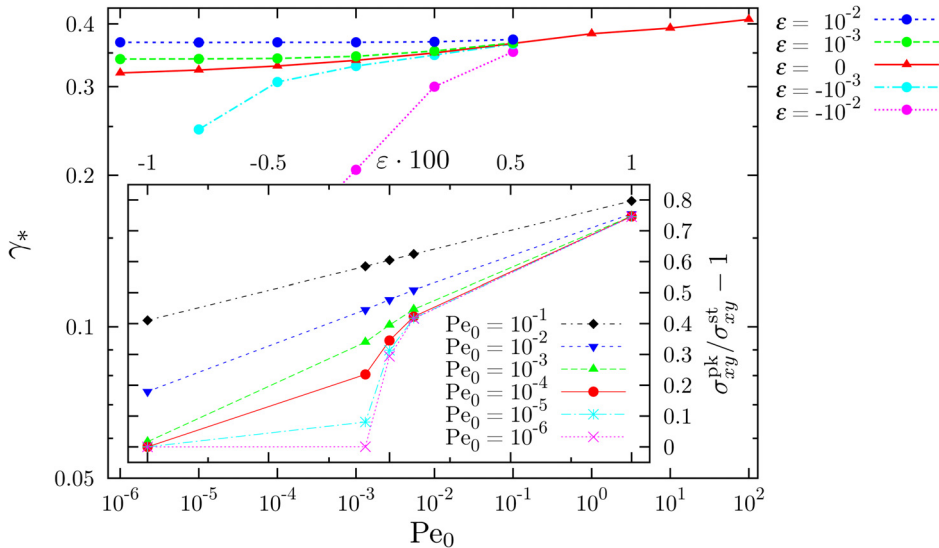


FIG. 5. The *main panel* shows peak strain values γ_* as a function of bare Péclet number Pe_0 . The grouping in separation parameters ε is given by the outside legend. The γ_{*s} are read off from the zeros of $g_{xy}(t, \dot{\gamma})$, Eq. (6). *Symbols* are connected with straight lines as guide for the eye. The *inset* shows the relative overshoot height $\sigma_{xy}^{pk}/\sigma_{xy}^{st} - 1$ of the MCT stress overshoots as function of separation parameters ε , grouped in bare Péclet numbers Pe_0 ; see inset legend. Both, peak positions and peak heights, increase with shear rate and with packing fraction.

overshoot allows to observe γ_* in the stress-strain curve directly. For the fluid state at $\varepsilon = -10^{-3}$, fitting a Kohlrausch law to the quiescent shear modulus $g_{xy}(t, 0)$ gives $\tau = 8063 d^2/D_0$ (and stretching exponent $\beta = 0.634$), so that $Wi = 1$ holds at bare Péclet number $Pe_0 = 1.24 \times 10^{-4}$. This corresponds well to the inset in Fig. 5, where one estimates a relative amplitude 0.238 (lin. interpolated) of the stress overshoot at this Péclet number. Decreasing Pe_0 further, the overshoot vanishes quickly. Except for this rapid variation when the quiescent fluid is approached, the position γ_* of the stress overshoot increases smoothly with packing fraction for all shear rates. This can be seen from the main panel of Fig. 5 and arises from the slight deepening of the undershoot in the shear modulus $g_{xy}(t, \dot{\gamma})$, which can be noticed in the inset of Fig. 3. The γ_* also is an increasing function of shear rate for all separations to the glass transition.

The overshoot's shape and height remain invariant, as long as internal relaxations play no role and parameters remain close to the glass transition, where τ is large. The inset of Fig. 5 shows that the relative overshoot height $\sigma_{xy}^{pk}/\sigma_{xy}^{st} - 1$, with σ_{xy}^{pk} the maximal stress value, increases with packing fraction and with Pe_0 outside the asymptotic regime. The former effect is due to the growth of the vertices and correlators in Eq. (6) with packing fraction, the latter due to the growing role of the β -decay with increasing shear rate. Note that the increase with density differs from the findings by Koumakis *et al.* (2012b), where the opposite was measured. A decrease of the relative overshoot height with packing fraction was attributed to approaching random close packing (RCP). Besides speculations by Amann *et al.* (2013), if ageing played a role, this difference remains unresolved. It may indicate that MCT-ITT does not describe the regime close to RCP, but around the glass transition, and that MCT's predictions fail at much higher or lower densities than at ϕ_c .

To illustrate the tensorial nature of the stress tensor $\boldsymbol{\sigma}(t)$ and of the 3d MCT-ITT approach, Fig. 6 shows a calculation of the first and second normal-stress differences $N_1(t) = \sigma_{xx}(t) - \sigma_{yy}(t)$ and $N_2(t) = \sigma_{yy}(t) - \sigma_{zz}(t)$. Already Brader *et al.* (2009) showed tensorial, numerical evaluations of $\boldsymbol{\sigma}(t)$ via a schematic MCT. However, in schematic MCT, $N_2 = 0$ under shear by construction. More recently, Farage *et al.* (2013) calculated for small shear rates the leading quadratic order of both normal stresses for stationary

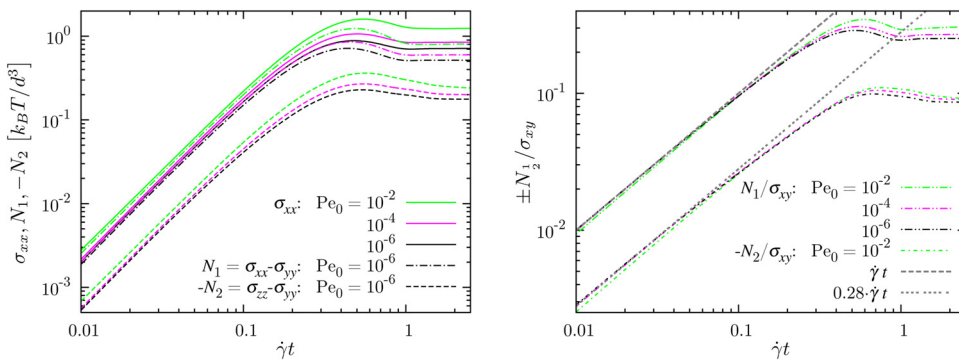


FIG. 6. Left panel: Transient normal stresses σ_{xx} (solid lines), first normal stress difference $N_1 = \sigma_{xx} - \sigma_{yy}$ (dotted dashed lines), and second normal stress difference $N_2 = \sigma_{yy} - \sigma_{zz}$ (dashed lines, plotted with negative sign) as functions of accumulated strain γt at the critical packing fraction ($\varepsilon = 0^+$) and for the Pe_0 s given in the legend (Pe_0 s are color coded for all line styles). One verifies that all $\sigma_{ii} > 0$ and $\sigma_{zz} > \sigma_{yy}$. Stress overshoots are apparent; they lie at 25% higher peak strains than in the shear stress. The right panel shows the normal stress differences divided by shear stress, N_1/σ_{xy} and $-N_2/\sigma_{xy}$, to illustrate the proportionality of this ratio to the accumulated strain in the elastic region. Gray dashed and gray dotted lines are linear fits with prefactors 1 and 0.28 (see legend).

flows in fluid states. Figure 6 shows results for the nonlinear regime of yielding glasses complementing their study.

Within MCT-ITT under simple shear, all components of the stress tensor can be calculated analogously to Eq. (4), by simply changing the components of some \mathbf{k} vectors. Because of the neglect of an isotropic contribution [Fuchs and Cates (2009)], however, the shear-dependent pressure cannot be calculated presently. Figure 6 shows the stress on a plane-element perpendicular to the flow direction, viz., $\sigma_{xx}(t)$, and the normal-stress differences as defined above, which are of distinguished rheological interest. The calculation has been done at the glass transition ($\varepsilon = 0^+$) and for $\text{Pe}_0 = 10^{-2}; 4; 6$, i.e., for a genuine, critical glass behavior with small Pe_0 and large Wi . The first observation is that they all exhibit a transient regime, with stress overshoots, which look qualitatively like those of the shear stress, cf. Fig. 2. The overshoots however occur at strains larger than 0.4, which is larger than all γ_* determined from the shear stress. At all times $t > 0$, it holds $\sigma_{xx} > \sigma_{zz} > \sigma_{yy} > 0$, which renders $N_1 > 0$ and $N_2 < 0$. Comparing more quantitatively, Brader *et al.* (2009) showed that the Lodge-Meissner relationship holds in the elastic regime. It reads $N_1(t)/\sigma_{xy}(t) = \gamma$, and states that the slope of the 1st normal-stress difference is quadratic in accumulated strain in the elastic regime with prefactor G_∞ , the shear modulus. The full 3d numerics recovers this relation and gives a corresponding one for the 2nd normal-stress difference: $N_2(t)/\sigma_{xy}(t) \approx -0.28\gamma$; both relations are shown in the right panel of Fig. 6. Outside the elastic regime, the simple linear relation between normal stresses and shear stress breaks down, as is clear from the different stress overshoot positions.

V. ATTRACTION DRIVEN GLASS

Turning on a SWP among the HSs, the attraction depth U relative to the thermal energy becomes an additional control variable. Increasing U the states diagram depends on the relative attraction range δ . We fix $\delta = 0.0465$, far smaller than Lindemann's ratio, in order to explore the consequences of physical bond-formation in concentrated dispersions. At this δ , the two different types of glass transitions, RDG and ADG, merge in an higher order singularity of MCT, denoted A_4 bifurcation point [Götze and Sperl (2002)]. This occurs around $U_{A_4} \approx 4.3$; see Fig. 1. For U below this value, the major effect of the attraction is to destabilize the RDG and to induce a (reentrant) fluid phase where equilibrium is reached at long times [Pham *et al.* (2002); Eckert and Bartsch (2002)]. For attractions close to and slightly above U_{A_4} (and concentrations below it), the ADG transition takes place where the short-ranged attraction causes cooperative bonding among caging particles. Even though the attraction strength is of the order of a few k_{BT} only, the "physical bonding" stabilizes a second nonergodic state with quite different mechanical properties than the RDG.

Figure 7 shows the (quiescent) shear moduli G_∞^c , viz., the elastic coefficients under volume conserving deformations, along the glass transition lines as functions of attraction strength U ; note that ϕ varies nonmonotonically along the red curve in Fig. 1 for these calculations. For $U = 0$ the modulus of HS indicated in Figs. 2 and 3 is recovered. At first, the attraction little changes the elastic shear modulus relative to the RDG value until around U_{A_4} , G_∞^c increases rapidly. For even shorter attraction range, e.g., $\delta = 0.03$, the modulus would jump discontinuously at the crossing of glass transition lines in Fig. 1 [Dawson *et al.* (2000)]. The mechanism causing the increase is the tighter localization of particles in the ADG than in the RDG. It remains an entropic effect like in the RDG, as $G_\infty^c \propto k_B T$, but asymptotically for small ranges MCT predicts an increase scaling like: $G_\infty^{\text{c,ADG}} \propto (1/\delta^2)G_\infty^{\text{c,RDG}}$. Note that for increasing U along the glass transition line (outside the range of Fig. 7) the elastic modulus decreases nonmonotonically, which was shown by Bergholtz *et al.* (2003). This happens because the particle concentration strongly

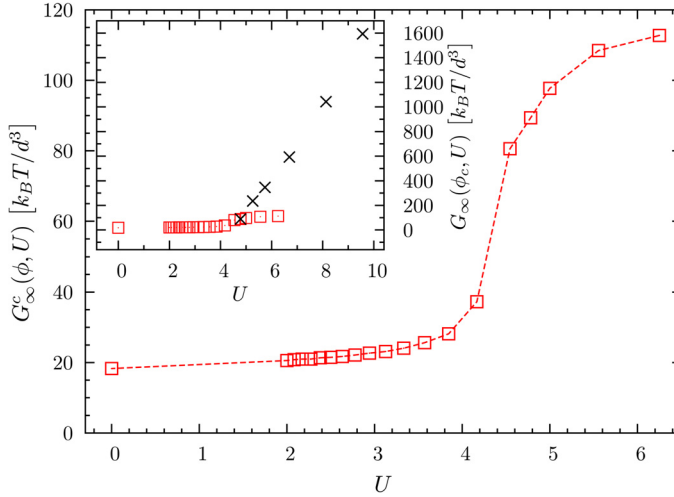


FIG. 7. Shear moduli of HSs with square well attraction of relative range $\delta = 0.0465$ as a function of attraction strength $U = u_0/k_B T$. Squares mark calculations along the glass transition line and correspond to the black squares in Fig. 1; the packing fraction ϕ_c varies nonmonotonically here. The inset shows shear moduli varying over a wider range. Symbols \times mark G_∞ calculated at fixed packing fraction ϕ_c and increasing U deeper into the attraction driven glass.

decreases along the transition line (and with it the elastic modulus) for increasing interaction strength.

Turning on shear destroys the elasticity of the amorphous solids and causes plastic deformations also in the presence of attractions. We choose the packing fraction ϕ_c given by the RDG transition of HS in order to study the interplay of attractions and shear. Figure 8 gives an overview of the stress-strain curves for various U . The HS curve is included and for the solid states the elastic law with the independently calculated linear shear moduli $G_\infty(\phi_c, U)$ from Fig. 7. Intermediate shear rates are chosen, in order to see strong effects but to remain well below the limit of applicability of MCT-ITT; recall that for HS, instabilities emerged for $Pe_0 > 10$. Starting the discussion of panel (a) in Fig. 8 in the elastic regime and at $U=0$, the linear region in the HS stress-strain curve lies somewhat above the linear elastic asymptote $G_\infty^{\text{RDG},\gamma}$ because the bare Péclet number is not asymptotically small; compare Fig. 2. For attraction strengths in the reentrant fluid region, the stress-strain relations clearly exhibit fluid behavior. At $U = U_c/2$ the glassy structure on intermediate time scales relaxes so fast that the stress-strain curve becomes monotonous as holds in linear viscoelastic response, where $g_{xy}(t)$ is independent of the shear rate. We estimate $Wi = \dot{\gamma}\tau \approx 0.015$ there, while it is infinite for $U=0$ and $U = U_c$. For the critical attraction strength U_c of the ADG, the stress-strain curve first exhibits a linear elastic regime, then an overshoot and finally a steady state. The linear regime is again well described by the asymptote $G_\infty^{\text{ADG},\gamma}$, yet, the linear shear modulus at the ADG transition exceeds the HS one by roughly a factor 4.9. The linear elastic response holds over a far smaller strain range than for HS, and the ensuing stress peak is far broader at the ADG than at the RDG transition. The physical bonds apparently start to get broken already at strains comparable to the attraction width so that plastic rearrangements occur and the linear elastic limit is left early. The position γ_* of the stress peak, however, is unexpectedly somewhat larger at the ADG than at the RDG transition. Yet bonds possibly by rotating and stretching still manage to bear stress up to strains even somewhat larger than characteristic for the RDG. Thus the stress overshoot is broad. Deep in the

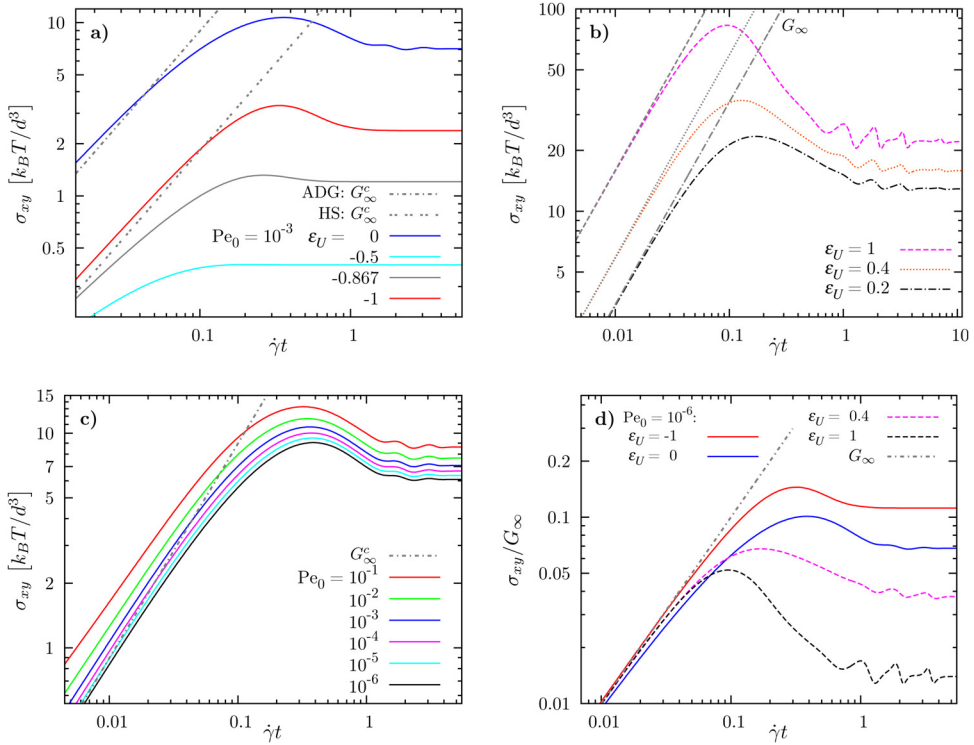


FIG. 8. Overview of the transient shear stress σ_{xy} vs accumulated strain $\dot{\gamma}t$ curves at fixed density when varying the attraction strength given by the relative separation to the critical attraction strength, $\epsilon_U = (U - U_c)/U_c$; the HS ϕ_c is chosen. In panel (a), $\epsilon_U = 1, 0.867, 0.5$, and 0 correspond to the HS case, two values in the reentrant fluid region, and at the attraction dominated transition; the shear rate is fixed at $Pe_0 = 10^{-3}$. In panel (b), $\epsilon_U = 0.2, 0.4$, and 1 (line style coded) enter deeper into the ADG. Here, calculations for Pe_0 between 10^{-6} and 10^{-1} overlap (master functions shown). Note, the oscillations upon reaching the steady state at the strongest U are due to the limitations of the rough q grid discretization. Panel (c) varies the shear rate as given in the legend at the ADG transition, $\epsilon_U = 0^+$. Panel (d) shows transient stresses divided by the corresponding shear moduli, $\sigma_{xy}(t)/G_\infty$ for some glass states (labeled by attraction strength separation ϵ_U). All curves overlap in the linear regime by construction as the shear rate is low, $Pe_0 = 10^{-6}$. In all panels, the elastic moduli G_∞ and G_∞^c , calculated from the plateaus of Figs. 3 and 9, or from Fig. 7, are shown as gray, dashed, dotted, or dashed dotted lines.

ADG, at twice the attraction strength than at the transition, the stress-strain curve exhibits the same regimes. Yet, the elastic modulus is larger and the position of the stress overshoot has shifted to noticeably smaller values. Also, the relative height of the overshoot has increased very strongly; see panel (b) in Fig. 8 and Fig. 11 below. Consequently, the steady state stress $\sigma_{xy}^{st}(\gamma \rightarrow \infty)$ is higher because of the steeper linear elastic increase, but lower than this effect would imply because of the large stress release after the maximal stress $\sigma_{xy}^{pk} = \sigma_{xy}(\gamma^*)$. This is brought out clearly in panel (d) of Fig. 8, where the stress divided by the shear modulus is shown for a representative set of attraction strengths. All curves overlap in the linear regime by construction. States affected by the short-ranged attraction leave the linear regime at very small strains, while the HS curve follows the linear elastic response far longer. The large fraction of stress released during yielding in states deep in the ADG is apparent, and the broadness of the stress overshoots with attractions. The transient stress curves at the high U also exhibit a broad maximum, which approaches the long-time limit only around strains of order unity. On top of this slow transient, the calculations in Fig. 8 exhibit noticeable oscillations which we consider artifacts of the coarse discretization of Eq. (6).

After this overview of the yielding and plastic deformation when turning on a short-ranged attraction, the different effects shall be explored in more detail. At first the region close to the critical attraction strength U_c shall be explored varying ε_U slightly, and second the behavior for large U is investigated. Finally, the steady state flow curves are presented. Recall that $\varepsilon_U = (U - U_c)/U_c$, i.e., $\varepsilon_U = -1$ in the HS case, $\varepsilon_U = 0$ at the ADG transition line, and $\varepsilon_U = \mathcal{O}(1)$ in the ADG glass region.

Panel (b) in Fig. 8 and Fig. 9 present a detailed look at the transient stress evolution close to the ADG transition where shear rate, nondimensionalized as bare Péclet number, and relative separation ε_U are varied. For attraction strengths close to the ADG, the linear elastic regime generally is followed by a stress maximum. Here, the linear elasticity only holds for rather small strains. Starting at strains below 5%, the stress grows sublinearly with strain. As the final approach to the steady state asymptote requires strains of order unity, in general a rather broad stress overshoot can be seen in the ADG. Comparing the relative magnitude of the stress overshoot and its strain-position γ_* , similar results are observed as in the HS case.

To support this comparison, Fig. 10 shows stress-peak strains γ_* and relative overshoot magnitudes $\sigma_{xy}^{\text{pk}}/\sigma_{xy}^{\text{st}} - 1$ for different ε_U and Pe_0 around the ADG and RDG transition. They correspond to the zeros and negative areas in Fig. 9, respectively. A noteworthy and at first unexpected effect is the larger characteristic strain value at the ADG than at the RDG. For shear rates giving $\text{Pe}_0 \leq 0.01$, the γ_* 's at the transition are somewhat larger for a glass where particles feel strong bonds to their neighbors than for a glass where repulsive interactions dominate. Close to the ADG, the characteristic strain γ_* does not correlate with the localization length, which is far smaller at the ADG than at the RDG as shown in the inset of Fig. 1. The cause of this subtle effect, which also depends on shear rate, is given by the extreme stretching of the quiescent α -process at this ADG transition.

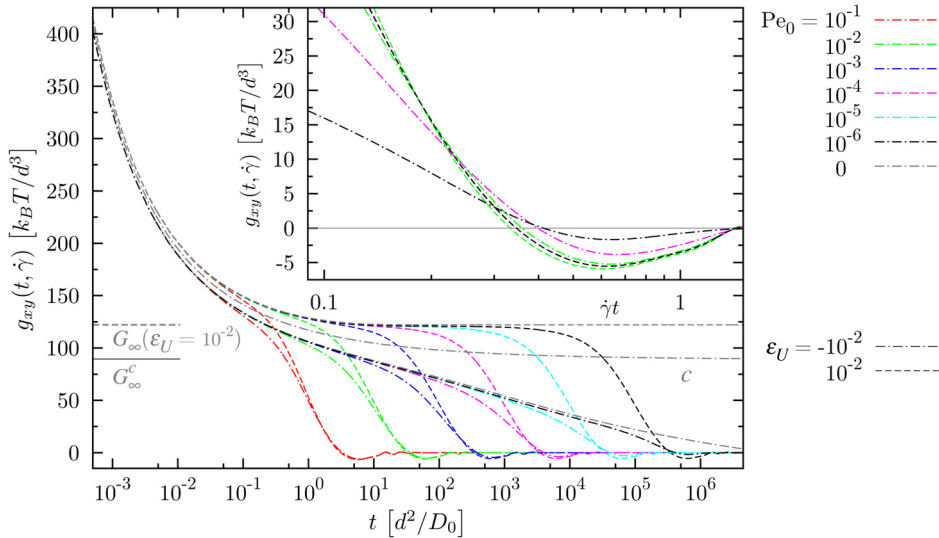


FIG. 9. Generalized shear modulus $g_{xy}(t, \gamma)$ of HSs with square well attraction close to the ADG transition, as function of time (*main panel*) and accumulated strain (*inset*; curves for every second Pe_0 left out for clarity). The legend provides *color coded* the strain rates and *line style coded* the relative attractions $\varepsilon_U = (U - U_c)/U_c$; all curves at the HS ϕ_c . A letter c labels the critical $g_{xy}(t, 0)$ for $\varepsilon_U = 0^+$. Elastic shear moduli $G_\infty(\varepsilon_U)$ can be read off from quiescent curves ($\text{Pe}_0 = 0$), with $G_\infty(\varepsilon = 0^+) = G_\infty^c = 89.5 k_B T / d^3$ and $G_\infty(\varepsilon = 10^{-2}) = 122 k_B T / d^3$. The *inset* shows subtle differences in the peak position γ_* , where $g_{xy}(t, \gamma) = 0$, which are caused by γ independent β and α decays; glass curves for $\text{Pe}_0 = 10^4$ and 10^6 overlap. For $\text{Pe}_0 = 10^6$ in the fluid, the undershoot (almost) disappears.

The *inset* shows subtle differences in the peak position γ_* , where $g_{xy}(t, \gamma) = 0$, which are caused by γ independent β and α decays; glass curves for $\text{Pe}_0 = 10^4$ and 10^6 overlap. For $\text{Pe}_0 = 10^6$ in the fluid, the undershoot (almost) disappears.

The physical cause was analyzed in detail by Götze and Sperl (2002): The scenario of two different glass transition lines causes very broad relaxation curves, culminating in logarithmic relaxation close to higher order glass transitions. At the present choice of density, attraction range and strength, the quiescent shear modulus happens to exhibit logarithmic decay for more than five decades; see Fig. 9. This causes a shear-distortion of the shear modulus around its zero which pushes γ_* to larger values. The inset of Fig. 9 shows the shallow negative region caused by the broad α -process for small shear rates. Thus γ_* increases for low Pe_0 . For larger shear rates the relaxation curves become steeper with larger U , and thus γ_* decreases entering the ADG. The extremely slow intrinsic relaxation also explains the broadness of the stress-overshoot because shear affects the internal relaxation in a wide time-window. This can also be deduced from the inset of Fig. 10, which shows that the stress overshoot exists for a broad window of shear rates at the ADG. Again this holds because the intrinsic α -process is characterized by a broad distribution of relaxation times. The broader crossover between a characteristically harder elastic regime and the steady state, reached after a larger plastic stress release, thus is the qualitative difference of the stress-strain curves at an attraction driven compared to a repulsion driven glass transition.

Figure 11 continues the investigation of Fig. 10, i.e., peak strain γ_* and relative overshoot magnitudes as function of ε_U and Pe_0 , but deep inside the ADG phase. There, the transient stress evolution changes strongly and in a characteristic way. First, the elastic constants G_∞ increase dramatically. The inset of Fig. 7 shows that at an attraction strength twice as large as the critical value of the ADG transition, the shear constant has increased by a factor around one hundred relative to the HS one. This can also be seen directly from the linear elastic regime in the stress-strain curves in Fig. 8(b). Nonlinearities set in at strain values comparable to the attraction range, as was observed at the ADG transition already.

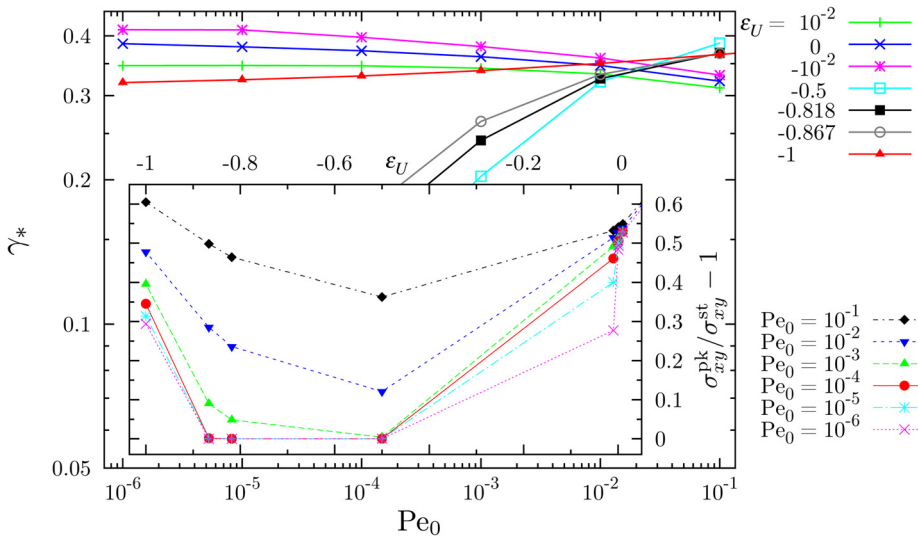


FIG. 10. The *main panel* shows peak strain values γ_* as function of bare Péclet number Pe_0 going from the HS glass transition ($\varepsilon_U = 1$) through the reentrant fluid state ($1 < \varepsilon_U < 0$) to the ADG transition ($\varepsilon_U = 0$); the packing fraction is fixed at ϕ_c . The upper outside legend gives the relative separations in attraction strength $\varepsilon_U = (U - U_c)/U_c$. The γ_* s are read off from the zeros of $g_{xy}(t, \gamma)$, Eq. (6). Symbols are connected with straight lines. The *inset* shows the relative overshoot height $\sigma_{xy}^{pk}/\sigma_{xy}^{st} - 1$ of the stress overshoots as function of the relative separation in attraction strength ε_U and for several Pe_0 (lower outside legend). The variations mainly result from the shift of the broad α process through the range set by the shear rate, with inverse temperature (similar to the HS case).

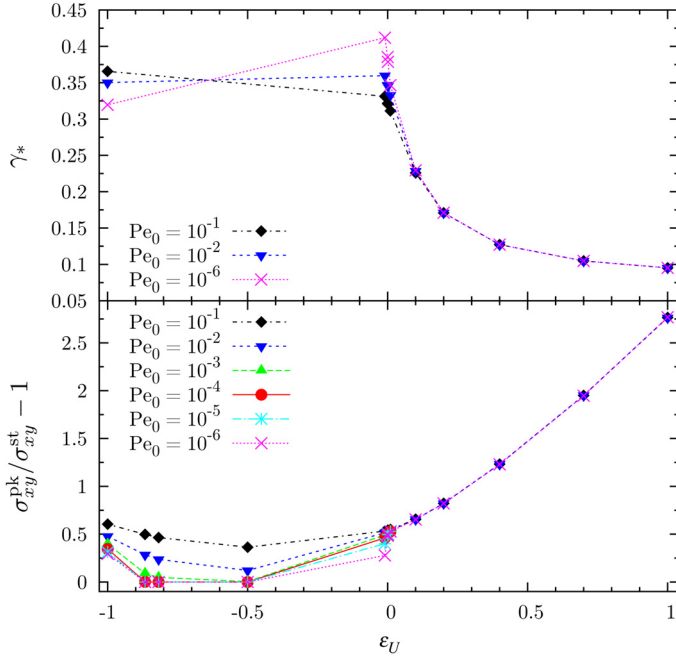


FIG. 11. Peak strain values γ_* (upper panel) as function of the relative separation in attraction strength $\varepsilon_U = (U - U_c)/U_c$ spanning from the HS glass transition, $\varepsilon_U = 1$, to the ADG transition, $\varepsilon_U = 0$, until deep in the ADG, $\varepsilon_U = -1$. The lower panel shows the relative overshoot height $\sigma_{xy}^{\text{pk}}/\sigma_{xy}^{\text{st}} - 1$ of the stress overshoots as function of ε_U . Data for several shear rates as shown as labeled with Pe_0 ; they overlap in the explored range.

Thus, deep inside the ADG phase where the overshoot peak is dominated completely by the elastic energy stored in the short range particle bonds (which is discussed in more detail together with Fig. 12 below), a bond reordering at smaller strain values shifts the peak position to much smaller γ_* for increasing U . The stress-overshoot retains its width in strain values, as the steady flow curve values is approached at accumulated strains of order unity (as we find for all considered states; recall that the wiggles in Fig. 8 at high U are numerical artifacts). This implies that the steady state stress then arises from a competition of shearing and repulsion dominated caging which is not very strongly affected by attractions. In consequence, a very prominent feature of the stress-overshoot deep in the attraction driven glass is its relative magnitude. The lower panel of Fig. 11 shows that the relative magnitude $\sigma_{xy}^{\text{pk}}/\sigma_{xy}^{\text{st}} - 1$ increases by around a factor six for the present path into the ADG. A large portion of the stress stored elastically for intermediate times is released during the late stage of the transient. The flow-curve deep in the ADG is raised by roughly a decade for the present parameters relative to the HS flow curve. This increase is smaller by a decade than the attraction driven increase of the elastic constant G_∞ . Because the internal β -relaxation at the states deep in the glass domain is quite rapid, no shear-rate dependence is observed in the stress-strain curves. This holds because the generalized shear modulus, which in general depends on time and strain independently, has become a function of accumulated strain only, $g_{xy}(t, \dot{\gamma}) = g_{xy}(t\dot{\gamma})$. Thus the stress-strain relations for different shear rates collapse onto a common master curve, which, for different U , are shown in Fig. 8 panel (b).

The structural rearrangements involved in the transient stress release around γ_* can be recognized from the wavevector dependent contributions in the generalized shear modulus. Figure 12 shows the wavevector dependent vertex, viz., the square bracket in Eq. (6), for some relevant attraction strengths U and densities. The strain values are (close to) the

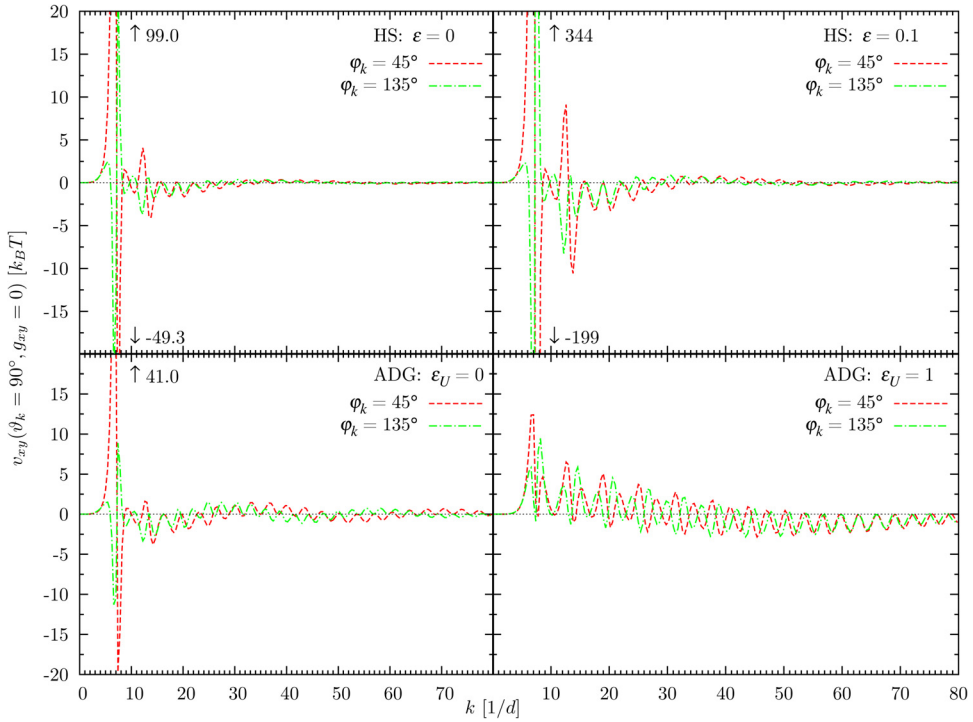


FIG. 12. Wavevector \mathbf{k} dependent vertex of the generalized shear modulus in Eq. (6); viz., the contents of the square bracket there. The directions of extensional ($\varphi_k = 45^\circ$, red, dashed lines) and compressional ($\varphi_k = 135^\circ$, green, dashed dotted lines) strain are chosen and the accumulated strain is (close) to γ_* . Four different glasses are considered as labeled and discussed in the text.

position γ_* of the stress overshoot. Two specific directions are chosen along the extensional ($\varphi_k = 45^\circ$) and compressional ($\varphi_k = 135^\circ$) axis, where the distortions of the structure are maximal under shear [Koumakis *et al.* (2012b)]. The correlators $\Phi_q(t)$ in Eq. (2) depend on time and accumulated strain independently. The former due to the intrinsic relaxation, the latter due to wavevector advection. In Eq. (6), the squared correlators are a weight for the purely strain/advection dependent vertex, and a stress overshoot emerges depending on the different weighting of wavevector contributions. If the product of structure factor deviations $S'_k S'_k(t)$ becomes negative for enough k values, the k -space integral and thus the shear modulus become negative. At the HS transition we recover the result which Zausch *et al.* (2008) obtained by isotropic averaging that negative contributions arise close to the principal peak of the static structure factor; for HS it lies close to $kd = 7$. The dominance of the principal peak in $S(k)$ at the RDG verifies that the RDG originates in the local steric packing always present in dense fluids. The origin of the stress-overshoot being negative contributions from the local order peak in $S(k)$, also holds deep in the RDG, viz., for HS at $\varepsilon = 0.1$, where the vertex has grown with density and varies more rapidly with wavevector, and where the corresponding density correlators are more glass like, viz., have higher plateau amplitudes. Figure 12 includes the vertex for $\varepsilon = 0.1$ to exemplify this; other results at this ε are not shown as they can be extrapolated based on the data presented in Sec. IV: For example, the characteristic strain has changed little relative to the HS transition at $\varepsilon = 0$, and takes the value $\gamma_*(\varepsilon = 0.1) = 0.33$ at $\text{Pe}_0 = 10^6$. Somewhat unexpectedly, the same wavevector range as at the RDG transition dominates the stress integral at the stress maximum of the ADG transition. This is shown in the panel at $\varepsilon_U = 0$ of Fig. 12. One notices that larger

wavevector contributions have grown, but the dominant contributions remains close to the peak in S_q . The large wavevector contributions in MCT-stress kernels capture the formation of physical bonds which result from the increased stickiness of the attractive SWP. It increases the equilibrium structure factor at large k . These high- k modes are responsible for the early breakdown of the linear elastic regime in ADG states; see Fig. 8. Nevertheless, the dominant contribution at the ADG transition remains connected with the local ordering of neighbor shells. Apparently, this is a universal characteristic of the yielding process of a glass at the transition in MCT-ITT. This holds even though the elastic modulus is characteristically larger at the ADG than at the RDG as shown in Fig. 7. The situation changes deep in the ADG at $U = 2U_c$ (i.e., $\varepsilon_U = 1$), where Fig. 12 indicates that negative contributions in the stress relaxation arise dominantly at large wavevectors. Then the characteristic strain γ_* becomes smaller, see Fig. 11, and the fraction of released stress grows strongly. This holds because the contributions at large wavevectors, viz., local rearrangements of the physical bonds, are rather rapid. When bond-formation and breakage dominate the stresses deep in the ADG, the advected wavevector changes quickly with time, and the vertices of MCT, which are positive only in the quiescent state, become negative rapidly. The presence of contributions from the main peak in S_q apparently cause that the bonded glass can rearrange (quasi) elastically until the packing-dominated cages yield. Then the stress is released, which was stored elastically in the physical bonds. As the bonds become distorted starting from very small strains, a characteristically broad stress-overshoot results. The vertex at $U = 2U_c$ in Fig. 12 is not decayed to zero at the upper cut-off in k of our integration. This indicates that the results at $\varepsilon_U = 1$ are not completely converged. Yet, we expect only quantitative corrections because of the evolution of results from smaller ε_U .

Figure 13 shows the flow curves for a few representative states spanning from the HS to the attraction driven glass transition and beyond, deep in the ADG. The packing fraction is kept fixed at the critical value of the HS transition, so that the $\varepsilon_U = -1$ curve

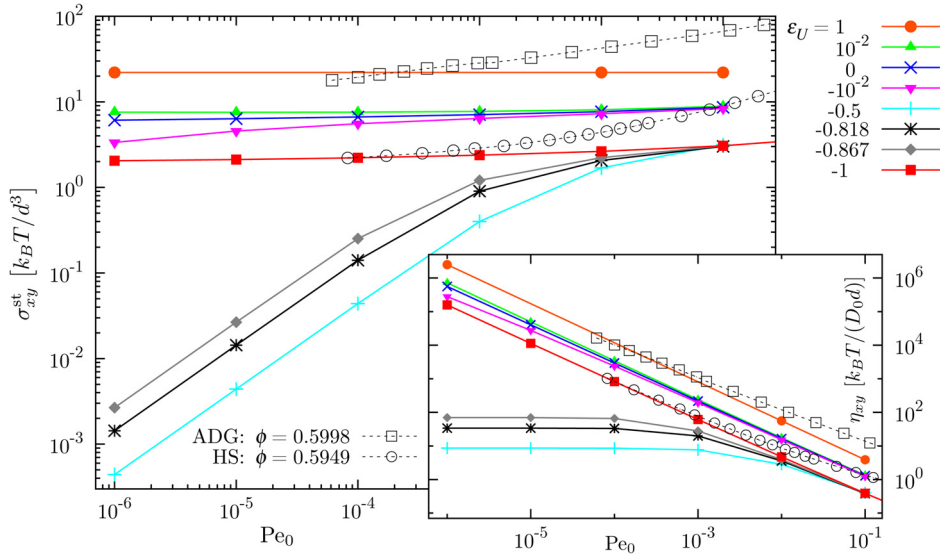


FIG. 13. The *main panel* shows flow curves $\sigma_{xy}(t \rightarrow \infty) = \sigma_{xy}^{\text{st}}$ vs bare Péclet number Pe_0 for relative attractions $\varepsilon_U = (U - U_c)/U_c$ as given in the legend. The curves span from the HS glass transition, $\varepsilon_U = -1$, to the ADG transition, $\varepsilon_U = 0$, until deep in the ADG, $\varepsilon_U = 1$. The *colored, full symbols* were calculated for six shear rates $Pe_0 \in \{10^{-6}, \dots, -1\}$ and are connected with straight lines as guides for the eye. The *hollow, black symbols* with packing fractions ϕ given in the legend are experimental data obtained by Pham *et al.* (2008). The comparison is discussed in Sec. VI. The *inset* shows the stationary viscosity $\eta_{xy} = \sigma_{xy}^{\text{st}}/\dot{\gamma}$.

corresponds to the critical HS curve at $\varepsilon = 0$ of Fig. 4, where flow curves of HSs were shown. The reentrant fluid region lies at small U , which correspond to negative separations $\varepsilon_U < 0$. The states from $\varepsilon_U = -0.867$ to $\varepsilon_U = -0.5$ exhibit Newtonian viscosities, which decrease with increasing U . Raising U up to close to the value of the ADG transition, the Newtonian viscosity increases again strongly. At, e.g., $\varepsilon_U = -0.01$, the Newtonian regime lies outside the window of Fig. 13 at lower bare Péclet numbers. Thus, crossing the reentrant liquid region, the Newtonian viscosity varies nonmonotonically as observed experimentally by Willenbacher *et al.* (2011). Entering the ADG, a yield stress σ_{xy}^+ arises as holds universally at MCT-ITT glass transitions. Comparing the values of σ_{xy}^+ at the HS and at the ADG transition at the same packing fraction ϕ_c , one notices an increase caused by the attractions. The yield stress increases by roughly the same factor as does the shear modulus G_∞ at both transitions; compare Fig. 7. Entering into the ADG, the steady stresses increase yet again. Because the local dynamics of caging and bonding has become quite fast according to MCT-ITT deep in the ADG, the flow-curve becomes shear-rate independent. At $\varepsilon_U > 0.1$, the numerical curves indicate no dependence on Pe_0 in the window of Fig. 13. It is noteworthy that the increase of the steady stress in the bonded glass relative to the HS glass is far smaller than the increase of the corresponding elastic constant. The inset of Fig. 7 indicates that G_∞ has hardened by around two orders when going from $U = 0$ to $U \approx 10$, while the yield stress increases only from around $\sigma_{xy}^+(U = 0) \approx 2k_B T/d^3$ to $\sigma_{xy}^+(U = 2U_c) \approx 22.0k_B T/d^3$. The reason behind the comparatively weak increase in the steady stress lies in the different stress recovery after imposing flow in the ADG and the RDG. A large fraction of the stress which is elastically stored in the physical bonds is released when the ADG fluidizes for strains of the order of γ_* ; see the overview of stress-strain curves in Fig. 8 and the detailed analysis of the magnitude of the stress-overshoot in Fig. 10.

Converting the flow curves into viscosities, $\eta_{xy} = \sigma_{xy}/\dot{\gamma}$, straightens out the curves over a wide range along the ordinate. The subtle sigmoidal shape of the flow curves of MCT-ITT close to a glass transition thus get ironed-out. The inset of Fig. 13 shows the corresponding viscosities which exhibit a Newtonian plateau in fluid states for small Weissenberg numbers and then cross over to shear-thinning with asymptotic exponent -1 . Restrictions in the numerical code prevent us also for the ADG to address the question of the existence of a second Newtonian plateau at high shear rates. The MCT-ITT calculations continue to decrease for the numerically accessible range of $\dot{\gamma}$.

Figure 14 shows the first and second normal-stress differences $N_1 = \sigma_{xx} - \sigma_{yy}$, $N_2 = \sigma_{yy} - \sigma_{zz}$. Choices in the numerical algorithm aimed at capturing strong flows give errors in

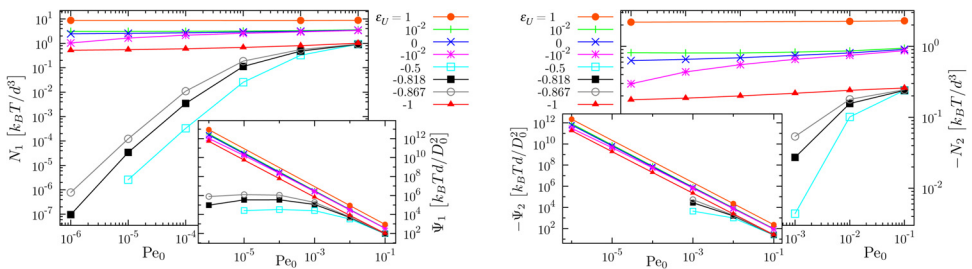


FIG. 14. The *left main panel* shows stationary first normal stress differences $N_1(t \rightarrow \infty) = \sigma_{xx}^{\text{st}} - \sigma_{yy}^{\text{st}}$ vs bare Péclet number Pe_0 for six shear rates $Pe_0 \in \{10^{-6}, \dots, 10^{-1}\}$ and for relative attractions $\varepsilon_U = (U - U_c)/U_c$ as given in the legend. The *Symbols* are connected with straight lines as guides to the eye. The *left inset* shows the first long time normal stress coefficient $\Psi_1 = (\sigma_{xx}^{\text{st}} - \sigma_{yy}^{\text{st}})/Pe_0^2$. The *right main panel* shows stationary second normal stress differences $N_2(t \rightarrow \infty) = \sigma_{yy}^{\text{st}} - \sigma_{zz}^{\text{st}}$, and its *inset* the corresponding long time normal stress coefficient $\Psi_2 = (\sigma_{yy}^{\text{st}} - \sigma_{zz}^{\text{st}})/Pe_0^2$.

the coefficients when they become too small in fluid states. Hence we cannot compare with the calculations by [Farage *et al.* \(2013\)](#) who considered the prefactor of the quadratic scaling at low Péclet numbers. As in the case of the shear stress, the steady state normal stresses deep in the ADG are above the ones of the HS at the same packing fraction. Yet, during the transient, again a large amount of the stress built-up during the linear elastic response is released upon yielding. The build-up of normal stresses during the deformation of physical bonds in the linear regime again obeys the Lodge-Meissner relationship as tested in [Fig. 6](#) for HSs; the tests for the ADG states are not shown.

VI. CONCLUSIONS AND COMPARISON WITH EXPERIMENTAL DATA

We presented the first fully quantitative solutions of the MCT-ITT equations for the nonlinear response of shear driven colloidal dispersions. The results on the transient shear stress response, the steady flow curves, and normal stresses at colloidal glass transitions exhibit the central qualitative features which have previously been discussed using schematic MCT-ITT models. They recover and quantify phenomena like the initial elastic response, which is linear in the accumulated strain, the yielding of glasses characterized by a dynamic yield stress, and the transient stress overshoot, which defines a strain γ_* characterizing the yielding process. Solutions of the MCT-ITT equations by [Henrich *et al.* \(2009\)](#), [Krüger *et al.* \(2011\)](#), and [Amann *et al.* \(2013\)](#) considering hard disks in two dimensions showed that these phenomena are universal at MCT-ITT glass transitions under shear and also arise in two-dimensional systems confined to a plane. These authors also discussed transient density correlators, tagged particle motion, and distorted structures, which, for three dimensions, can only be presented in future. The present three-dimensional solutions, however, enable comparison with experimental data, which are available for dispersions of colloidal HSs and of colloids mixed with nonadsorbing polymers which induce a short-ranged attraction of Asakura-Oosawa form.

A quite stringent comparison of the theoretical results for HSs in [Sec. IV](#) can be made with the experiments by [Crassous *et al.* \(2008\)](#) who studied core-shell particles consisting of a polystyrene core and a thermosensitive, crosslinked PNIPAM shell. The microgel dispersions with size polydispersity of 9.3% can be mapped onto the phase diagram of monodisperse HSs using the freezing density $\phi_F = 0.494$ and exhibit the strongest tendency to crystallize around $\phi_{\text{eff}} = 0.55$. The rheology at higher packing fractions closer to vitrification appears little affected by crystallization. The effective packing fraction can be adjusted by changing the weight percentage of particles or by changing the effective size R_H (viz., the hydrodynamic radius taken to be $d/2$ here) by temperature, which makes it possible to approach the glass transition packing fraction of HSs $\phi_c = 0.58$ quite closely. Moreover, the frequency-dependent linear response moduli $G'(\omega)$ and $G''(\omega)$ were already quantitatively analyzed using MCT so that the mapping of the theory onto the rheology is known. [Crassous *et al.* \(2008\)](#) found that roughly the same value of the critical packing fraction as established by [[Pusey and van Megen \(1987\)](#)] studying poly(methyl methacrylate) (PMMA) HS colloids using dynamic light scattering rationalizes the microgel rheology. The separation parameters obtained by [Crassous *et al.* \(2008\)](#) and listed in the caption of [Fig. 4](#) refer to this experimental HS glass transition density. Clearly, the theoretical results, which are calculated (not fitted) for comparable separation parameters from the theoretical ϕ_c , show quite comparable flow curves. The need to use the separation from the critical packing fraction instead of the actual value of the packing fraction in order to compare MCT and experiment is well established [[Götze \(2009\)](#)]. It arises from the approximate nature of MCT which misses the precise value of ϕ_c , while capturing the sensitive dependence of the viscoelasticity on the separation to the

glass transition. The comparison in Fig. 4 can in principle be done without adjustable parameter, because D_0 sets the time scale in Eq. (2) and can be calculated from the solvent viscosity following Stokes, Einstein, and Sutherland [Einstein (1905); Sutherland, (1905)]. Also the stresses are calculated directly. Yet, hydrodynamic interactions are neglected by MCT-ITT. They affect the short time diffusion coefficient, which at high concentrations is a more relevant scale than the Stokes-Einstein-Sutherland diffusion coefficient at infinite dilution. Additionally, hydrodynamic interactions add a contribution to the viscosity at high shear rates. Crassous *et al.* (2008) found that the linear moduli agree best when assuming that the hydrodynamic interactions slow down the short time diffusion to $0.15 D_0$. (The viscosity $\eta_\infty^{\dot{\gamma}}$ observed at high shear rates is indicated in Fig. 4 to describe the second origin of hydrodynamic deviations.) Also they observed that MCT underestimates stresses by 40% (a rescaling factor $c_y^G = 1.4$ was used). The data in Fig. 4 were rescaled by the given ratio of the diffusion coefficients, but by a different stress-rescaling factor: $c_y^\sigma = 0.55$. Quite satisfactorily MCT deviates by less than 50% from either experiment. The aspect that theory underestimates the linear elastic stress but overestimates the steady state stress of the yielding glass can be traced back to the error of MCT-ITT in determining the characteristic strain value γ_* . While transient stress-strain curves are not available for the microgel dispersions by Crassous *et al.* (2008), stress-overshoots were measured in more polydisperse microgel samples. Amann *et al.* (2013) measured $\gamma_*^{\text{ex}} \approx 0.10$ while our MCT-ITT calculation gives $\gamma_*^{\text{mct}} \approx 0.32$. Apparently, MCT-ITT underestimates the speedup by shear of stress fluctuations. While experiments close to the glass transition in HS colloids, including the large amplitude oscillatory measurements by Petekidis *et al.* (2002), find characteristic strain values around 10%, MCT-ITT overestimates it by a factor around three. Consequently the steady stresses are somewhat overestimated, even though the linear elastic regime is somewhat underestimated. Reassuringly, the deviations by MCT-ITT in three dimensions are appreciably smaller than the deviations in two-dimensional hard disk systems, where Henrich *et al.* (2009) found larger correction factors of the flow curves; they found around $c_y^\sigma = 0.1$. Considering the density dependence of the stress-overshoot peak-strain γ_* , one notices a similar increase than found by Petekidis *et al.* (2002) for the strain where irreversible rearrangements first appear in states close to the glass transition. Intriguingly, their light scattering measurements of this characteristic strain reveal a maximum at intermediate densities followed by a decrease when approaching RCP. The dependence of γ_* on packing fraction thus is richer than the dependence of the localization length on ϕ . The latter is expected to be monotonically decreasing with higher packing fraction as particles get localized more tightly. While both length scales thus characterize the cage effect in RDG transitions, and take comparable values right at the HS glass transition, their precise relation is nonlinear and not straightforward.

Turning on the short-ranged attractions by adding polymer to the colloids, first the states diagram can be tested. It consists of two different glass states, a reentrant fluid region, and possibly glass-to-glass transitions and higher order glass singularities. Pham *et al.* (2002) and Eckert and Bartsch (2002) found qualitative agreement concerning the transition lines, with the ones from theory shifted, but tracking the experimental ones. Willenbacher *et al.* (2011) extended these studies by pushing the reentrant fluid region to higher packing fractions. The enhanced elastic stiffness of the glasses with physical bonds was convincingly seen by Pham *et al.* (2006) and Pham *et al.* (2008). While stress vs strain curves after shear start-up are not available, Pham *et al.* (2008) present and discuss as equivalent stresses after step strain deformations. The observed characteristic strain $\gamma_* \approx 0.1$ for HSs corresponds well to the above discussion. For glasses with a polymer-induced attraction of roughly 6% range, the stress-strain relations show two characteristic differences to the ones of HSs. First, nonlinear deviations to the linear elastic response set in at rather small strain values. This, considering the differences in

attraction potential, agrees well with our findings from MCT-ITT. The origin of the nonlinearities lies in the high-wavevector contributions of the memory kernels which cause a broadly stretched quiescent structural relaxation. They also are very susceptible to wavevector advection, the mechanism by which shear affects the structural relaxation in MCT-ITT. Thus small strains suffice to soften the elastic response. The second experimental finding is a second maximum of the stress at strain values beyond one, which is not observed by MCT-ITT. The stress maximum at large strains is higher than the maximum at strains comparable to the repulsive case, distorting it to a shoulder. While MCT-ITT appears to capture the phenomena at the first characteristic strain γ_* which remains close to the HS value, the second stress maximum is missed. Presumably, it arises from structural correlations in the bonded glassy state which reach beyond the cage-effect length scale. Going to the final steady state, Fig. 13 contains the experimental flow curves obtained by Pham *et al.* (2008) for a repulsion and an ADG state. The experimental data are mapped onto the theoretical calculations by estimating the diffusion coefficient $D_0 = k_B T / (3\pi\eta_{\text{solv}}d)$ by using $\eta_{\text{solv}} = 1 \text{ mPa s}$ with the particle size $d = 260 \text{ nm}$. For the PMMA HS colloids in an organic solvent a slightly different stress-rescaling factor needs to be used than in Fig. 4. The value $c_y^\sigma = 3.05$ gives the best agreement for the HS data. After this mapping of the HS data, the increase of the yield stress deep in an ADG state can be addressed in Fig. 13. While the differences in packing fraction, attraction range and strength prevent a more detailed comparison, the hardening of the flow curves at (roughly) fixed packing fraction upon increasing the attraction strength agrees qualitatively with the MCT-ITT calculation. A more detailed comparison appears justified, which would require improved equilibrium structural input.

Based on the encouraging comparisons of the nonlinear stress-strain relations from microscopic MCT-ITT with experiments on model colloidal systems, it appears worthwhile to consider shear-distorted structure and transient density correlations in order to gain a deeper understanding of the mechanisms of plastic deformation and yielding of colloidal glasses. Work along these lines is underway.

ACKNOWLEDGMENTS

The authors thank Th. Voigtmann for valuable discussions, M. Siebenbürger for help in interpreting the experimental data, and the Deutsche Forschungsgemeinschaft (DFG) for financial support in the initiative FOR 1394, project P3.

APPENDIX: NUMERICAL IMPLEMENTATION

In this appendix, the numerical implementation of MCT-ITT in three dimensions is summarized. The standard challenge to solve MCT-equations over around ten decades in time is made more difficult by the requirement to compute $2 \cdot d$ dimensional wavevector integrals for the memory kernels. Desirable requirements to the numerics are to recover an isotropic quiescent solution [Fransosch *et al.* (1997)], while choosing a sufficiently close \mathbf{q} -grid discretization in Fourier space, in order to minimize discretization errors.

The numerical evaluation of Eq. (2) depends mainly on the discretization of the friction kernel $m_q(t, t')$ in Eq. (3). Under simple start-up shear, the dependence on two times t and $t' < t$ can be simplified on the dependence on the time interval $\tau = t - t'$, yielding $m_{\mathbf{q}(\mathbf{v})}(\tau)$, which is explained in detail by Fuchs and Cates (2009). This yields a so called single-time MCT, which is far simpler to solve than two-times MCT considered by Voigtmann *et al.* (2012). The temporal evaluation of Eq. (2) follows the standard scheme

TABLE I. Generic parameters of the \mathbf{q} grid used for this work. ϕ_c is rounded up in the seventh digit.

HS q	ADG q	Δq	$2\pi/\Delta\varphi_q$	$\pi/\Delta\vartheta_q$	HS ϕ_c
[0.2;39.8]	[0.2;79.8]	0.4	24	24	0.515712(1)

of previous MCT-ITT calculations (also schematic MCT) and is described in detail, e.g., by Voigtmann *et al.* (2012) and Amann (2013). The temporal discretization is performed on a time grid consisting of blocks, which each consist of $N_t = 64$ linearly spaced time instances. A straightforward discretization backward in time [see Brader-Voigtmann algorithm [Amann (2013)]] and $\Phi_{\mathbf{q}}(t)$ is iteratively solved, depending on all time instances $t' \leq t$. The first time block is initialized by $\Phi_{\mathbf{q}} = \exp(-\Gamma_{\mathbf{q}}t)$. As second input, the PY structure factor for HSs and square well potentials is used [Hansen and McDonald (2009); Baxter (1970); Dawson *et al.* (2000)]. Subsequent time blocks are generated by doubling the time step and using the arithmetic average of $\Phi_{\mathbf{q}}$ and $m_{\mathbf{q}}(t)$ of two instances of the preceding time block to initialize the first $N_t/2$ instances of the new time block. Via this decimation procedure, a large time range can be covered.

The discretization of wavevectors in \mathbf{q} space [and the \mathbf{k} integral in the friction kernel, Eq. (3)] has been performed using standard spherical coordinates, $\mathbf{q} = (q_x q_y q_z) = q(\cos\varphi_q \sin\vartheta_q \sin\varphi_q \sin\vartheta_q \cos\vartheta_q)$, discretizing modulus q , azimuthal angle φ_q , and inclination angle ϑ_q . This helps to keep the isotropy in quiescent calculations and simplifies identifying spherical symmetries in the computed observables. Under shear however, the \mathbf{q} grid becomes completely anisotropic in three dimensions. The $V_{\mathbf{q}\mathbf{k}\mathbf{p}}(t)$ is $2 \cdot d$ dimensional. The computation of $\mathbf{k}(t)$ respects shear advection via coordinate transformations and depends on the according $\mathbf{q}(t=0)$, which has been chosen as k_z axis; see Amann (2013) for more details. Table I shows the generic parameter choice used for the computation of the results of this work as best trade-off between computation time and precision.

With *OpenMP* parallelization on 32 CPUs á 2.6 GHz and 66 GB RAM, the calculation of one stress-strain curve in the ADG takes up to 90 h. Only the repeated calculation of $m_{\mathbf{q}(\nu)}(\tau)$ can be parallelized effectively to gain computation speed. Hence, a compromise in precision and computation time must be accepted. A method of saving computation time in the iteration of $\Phi_{\mathbf{q}}(t)$, which needs a repeated calculation of $m_{\mathbf{q}(\nu)}(\tau)$, is to store the vertex for the youngest time instance t , which consumes a relevant fraction of the available RAM and limits the grid discretization. Thus, RAM consumption and computation time increase approximately with the square of the grid-point density.

References

- Amann, C. P., “Time dependent flows in arrested states,” Ph.D. thesis, Universitat Konstanz, 2013.
- Amann, C. P., F. Weysser, M. Fuchs, M. Siebenburger, M. Ballauff, and M. Kruger, “Overshoots in stress strain curves: Colloid experiments and schematic mode coupling theory,” *J. Rheol.* **57**, 149–175 (2013).
- Ballauff, M., J. M. Brader, S. U. Egelhaaf, M. Fuchs, J. Horbach, N. Koumakis, M. Kruger, M. Laurati, K. J. Mutch, G. Petekidis, M. Siebenburger, Th. Voigtmann, and J. Zausch, “Residual stresses in glasses,” *Phys. Rev. Lett.* **110**, 215701 (2013).
- Baxter, R. J., “Ornstein Zernike relation and Percus Yevick approximation for fluid mixtures,” *J. Chem. Phys.* **52**, 4559–4562 (1970).
- Bergenholtz, J., and M. Fuchs, “Nonergodicity transitions in colloidal suspensions with attractive interactions,” *Phys. Rev. E* **59**, 5706–5715 (1999).
- Bergenholtz, J., M. Fuchs, and Th. Voigtmann, “Colloidal gelation and non ergodicity transitions,” *J. Phys.: Condens. Matter* **12**, 6575–6583 (2000).

- Bergenholtz, J., W. C. K. Poon, and M. Fuchs, "Gelation in model colloid polymer mixtures," *Langmuir* **19**, 4493–4503 (2003).
- Brader, J. M., M. E. Cates, and M. Fuchs, "First principles constitutive equation for suspension rheology," *Phys. Rev. E* **86**, 021403 (2012).
- Brader, J. M., Th. Voigtmann, M. Fuchs, R. G. Larson, and M. E. Cates, "Glass rheology: From mode coupling theory to a dynamical yield criterion," *Proc. Natl. Acad. Sci. U.S.A.* **106**, 15186–15191 (2009).
- Crassous, J. J., M. Siebenbueger, M. Ballauff, M. Drechsler, D. Hajnal, O. Henrich, and M. Fuchs, "Shear stresses of colloidal dispersions at the glass transition in equilibrium and in flow," *J. Chem. Phys.* **128**, 204902 (2008).
- Dawson, K., G. Foffi, M. Fuchs, W. Gotze, F. Sciortino, M. Sperl, P. Tartaglia, Th. Voigtmann, and E. Zaccarelli, "Higher order glass transition singularities in colloidal systems with attractive interactions," *Phys. Rev. E* **63**, 011401 (2000).
- Eckert, T., and E. Bartsch, "Re-entrant glass transition in a colloid polymer mixture with depletion attractions," *Phys. Rev. Lett.* **89**, 125701 (2002).
- Einstein, A., "Über die von der molekularkinetischen theorie der warme geforderte bewegung von in ruhenden flussigkeiten suspendierten teilchen," *Ann. Phys.* **17**, 549–560 (1905).
- Fabbian, L., W. Gotze, F. Sciortino, P. Tartaglia, and F. Thiery, "Ideal glass glass transitions and logarithmic decay of correlations in a simple system," *Phys. Rev. E* **59**, R1347(R) (1999).
- Farage, T. F. F., J. Reinhardt, and J. M. Brader, "Normal stress coefficients and rod climbing in colloidal dispersions," *Phys. Rev. E* **88**, 042303 (2013).
- Franosch, T., M. Fuchs, W. Gotze, M. R. Mayr, and A. P. Singh, "Asymptotic laws and preasymptotic correction formulas for the relaxation near glass transition singularities," *Phys. Rev. E* **55**, 7153–7176 (1997).
- Fuchs, M., "Nonlinear rheological properties of dense colloidal dispersions close to a glass transition under steady shear," *Adv. Polym. Sci.* **236**, 55–115 (2010).
- Fuchs, M., and M. E. Cates, "Theory of nonlinear rheology and yielding of dense colloidal suspensions," *Phys. Rev. Lett.* **89**, 248304 (2002).
- Fuchs, M., and M. E. Cates, "A mode coupling theory for Brownian particles in homogeneous steady shear flow," *J. Rheol.* **53**, 957–1000 (2009).
- Gadala Maria, F., and A. Acrivos, "Shear induced structure in a concentrated suspension of solid spheres," *J. Rheol.* **24**, 799–814 (1980).
- Gibaud, T., F. Cardinaux, J. Bergenholtz, A. Stradner, and P. Schurtenberger, "Phase separation and dynamical arrest for particles interacting with mixed potentials the case of globular proteins revisited," *Soft Matter* **7**, 857–860 (2011).
- Gotze, W., *Complex Dynamics of Glass Forming Liquids – A Mode Coupling Theory* (Oxford University Press, New York (2009)).
- Gotze, W., and M. Sperl, "Logarithmic relaxation in glass forming systems," *Phys. Rev. E* **66**, 011405 (2002).
- Hajnal, D., and M. Fuchs, "Flow curves of colloidal dispersions close to the glass transition asymptotic scaling laws in a schematic model of mode coupling theory," *Eur. Phys. J. E* **28**, 125–138 (2009).
- Hansen, J., and I. McDonald, *Theory of Simple Liquids*, 3rd ed. (Academic, London, 2009).
- Henrich, O., F. Weysser, M. E. Cates, and M. Fuchs, "Hard discs under steady shear: Comparison of Brownian dynamics simulations and mode coupling theory," *Phil. Trans. R. Soc. A* **367**, 5033–5050 (2009).
- Hunter, G. L., and E. R. Weeks, "The physics of the colloidal glass transition," *Rep. Prog. Phys.* **75**, 066501 (2012).
- Kim, J. M., J. Fang, A. P. R. Eberle, R. Castaneda Priego, and N. J. Wagner, "Gel transition in adhesive hard sphere colloidal dispersions: The role of gravitational effects," *Phys. Rev. Lett.* **110**, 208302 (2013).
- Koumakis, N., and G. Petekidis, "Two step yielding in attractive colloids: Transition from gels to attractive glasses," *Soft Matter* **7**, 2456–2470 (2011).
- Koumakis, N., A. Pamvouxoglou, A. S. Poulos, and G. Petekidis, "Direct comparison of the rheology of model hard and soft particle glasses," *Soft Matter* **8**, 4271–4284 (2012a).
- Koumakis, N., M. Laurati, S. U. Egelhaaf, J. F. Brady, and G. Petekidis, "Yielding of hard sphere glasses during start up shear," *Phys. Rev. Lett.* **108**, 098303 (2012b).
- Kruger, M., F. Weysser, and M. Fuchs, "Tagged particle motion in glassy systems under shear: Comparison of mode coupling theory and Brownian dynamics simulations," *Eur. Phys. J. E* **34**, 1–22 (2011).

- Lekkerkerker, H., W. Poon, P. Pusey, A. Stroobants, and P. Warren, "Phase behaviour of colloid + polymer mixtures," *Europhys. Lett.* **20**, 559–564 (1992).
- Lindemann, F. A., "Über die Berechnung molekularer Eigenfrequenzen," *Physik. Z.* **11**, 609–612 (1910).
- Lu, P. J., E. Zaccarelli, F. Ciulla, A. B. Schofield, F. Sciortino, and D. A. Weitz, "Gelation of particles with short range attraction," *Nature* **453**, 499–503 (2008).
- Miyazaki, K., D. R. Reichman, and R. Yamamoto, "Supercooled liquids under shear: Theory and simulation," *Phys. Rev. E* **70**, 011501 (2004).
- Petekidis, G., A. Moussaid, and P. Pusey, "Rearrangements in hard sphere glasses under oscillatory shear strain," *Phys. Rev. E* **66**, 051402 (2002).
- Pham, K. N., A. M. Puertas, J. Bergenholtz, S. U. Egelhaaf, A. Moussaid, P. N. Pusey, A. B. Schofield, M. E. Cates, M. Fuchs, and W. C. K. Poon, "Multiple glassy states in a simple model system," *Science* **296**, 104–106 (2002).
- Pham, K. N., G. Petekidis, D. Vlassopoulos, S. U. Egelhaaf, P. N. Pusey, and W. C. K. Poon, "Yielding of colloidal glasses," *Europhys. Lett.* **75**, 624–630 (2006).
- Pham, K. N., G. Petekidis, D. Vlassopoulos, S. U. Egelhaaf, W. C. K. Poon, and P. N. Pusey, "Yielding behavior of repulsion and attraction dominated colloidal glasses," *J. Rheol.* **52**, 649–676 (2008).
- Priya, M., and Th. Voigtmann, "Nonlinear rheology of dense colloidal systems with short ranged attraction: A mode coupling theory analysis," *J. Rheol.* **58**, 1163–1187 (2014).
- Puertas, A. M., C. D. Michele, F. Sciortino, P. Tartaglia, and E. Zaccarelli, "Viscoelasticity and stokes Einstein relation in repulsive and attractive colloidal glasses," *J. Chem. Phys.* **127**, 144906 (2007).
- Puertas, A. M., M. Fuchs, and M. E. Cates, "Comparative simulation study of colloidal gels and glasses," *Phys. Rev. Lett.* **88**, 098301 (2002).
- Pusey, P. N., and W. van Megen, "Observation of a glass transition in suspensions of spherical colloidal particles," *Phys. Rev. Lett.* **59**, 2083–2086 (1987).
- Siebenburger, M., M. Fuchs, H. Winter, and M. Ballauff, "Viscoelasticity and shear flow of concentrated, non-crystallizing colloidal suspensions: Comparison with mode coupling theory," *J. Rheol.* **53**, 707–726 (2009).
- Siebenburger, M., M. Fuchs, and M. Ballauff, "Viscoelasticity and shear flow of concentrated, noncrystallizing colloidal suspensions: Comparison with mode coupling theory," *Soft Matter* **8**, 4014–4024 (2012).
- Sutherland, W., "Dynamical theory of diffusion for non electrolytes and the molecular mass of albumin," *Philos. Mag.* **9**, 781–785 (1905).
- van Megen, W., and S. M. Underwood, "Glass transition in colloidal hard spheres: Mode coupling theory analysis," *Phys. Rev. Lett.* **70**, 2766–2769 (1993).
- Voigtmann, Th., J. M. Brader, M. Fuchs, and M. E. Cates, "Schematic mode coupling theory of glass rheology: Single and double step strains," *Soft Matter* **8**, 4244–4254 (2012).
- Willenbacher, N., J. S. Vesaratchanon, O. Thorwarth, and E. Bartsch, "An alternative route to highly concentrated, freely flowing colloidal dispersions," *Soft Matter* **7**, 5777–5788 (2011).
- Zaccarelli, E., and W. C. K. Poon, "Colloidal glasses and gels: The interplay of bonding and caging," *Proc. Natl. Acad. Sci. U.S.A.* **106**, 15203–15208 (2009).
- Zausch, J., J. Horbach, M. Laurati, S. U. Egelhaaf, J. M. Brader, Th. Voigtmann, and M. Fuchs, "From equilibrium to steady state: The transient dynamics of colloidal liquids under shear," *J. Phys.: Condens. Matter* **20**, 404210 (2008).